Supplementary Information

Taming salophen in rare earth metallocene chemistry

Ernesto Castellanos, Florian Benner, and Selvan Demir*

Department of Chemistry, Michigan State University, 578 South Shaw Lane, East Lansing, Michigan 48824, USA

*Correspondence to: sdemir@chemistry.msu.edu (S.D.)

Inorg. Chem. Front.

Table of Contents

1 X-Ray Crystallography

Table S1. Crystallographic Data and Structural Refinements of $(Cp^*_2RE)_2(\mu\text{-}^{tBu}salophen)\bullet 3tol$, where RE = Gd (**1**), Dy (**2**), and Y (**3**).

	Gd (1)	**Dy (2)**	**Y (3)**
Empirical formula	$C_{97}H_{130}Gd_2N_2O_2$	$C_{97}H_{130}Dy_2N_2O_2$	$C_{97}H_{130}N_2O_2Y_2$
Formula weight	1670.52	1681.02	1533.84
Temperature/K	100.00(10)	100.00(10)	100.00(10)
Crystal system	Triclinic	triclinic	triclinic
Space group	P−*1*	P−*1*	P−*1*
a/Å	13.29159(18)	13.30200(10)	13.2958(2)
b/Å	17.9159(3)	17.8838(2)	17.8857(3)
c/Å	18.6270(3)	18.6222(2)	18.6124(3)
α/°	74.8284(11)	74.7980(10)	74.7606(14)
β/°	84.4183(11)	84.3290(10)	84.4318(15)
γ/°	87.0897(10)	87.2430(10)	87.1630(14)
Volume/Å^3	4259.29(12)	4252.96(8)	4249.00(12)
Z	2	2	2
ρ_{calc} g/cm^3	1.303	1.313	1.199
μ/mm^{-1}	1.592	9.648	1.407
F(000)	1740.0	1748.0	1640.0
Crystal size/mm^3	0.118 × 0.091 × 0.07	0.258 × 0.147 × 0.134	0.456 × 0.389 × 0.266
Radiation	Mo K_α (λ = 0.71073)	Cu K_α (λ = 1.54184)	Mo K_α (λ = 0.71073)
2Θ range for data collection/°	4.364 to 62.412	4.938 to 154.584	4.552 to 58.106
Index ranges	$-18 \le h \le 16$, $-23 \le k \le 22$, $-24 \le l \le 23$	$-16 \le h \le 16$, $-19 \le k \le 22$, $-22 \le l \le 23$	$-16 \le h \le 17$, $-24 \le k \le 23$, $-25 \le l \le 24$
Reflections collected	74383	108689	62261
Independent reflections	21857 [R_{int} = 0.0497, R_σ = 0.0491]	17571 [R_{int} = 0.0564, R_σ = 0.0325]	19985 [R_{int} = 0.0275, R_σ = 0.0348]
Data/restraints/parameters	21857/0/962	17571/0/962	19985/0/962
Goodness-of-fit on F^2	1.034	1.061	1.039
Final R indexes [$I >= 2\sigma(I)$]	R_1 = 0.0357, wR_2 = 0.0823	R_1 = 0.0607, wR_2 = 0.1671	R_1 = 0.0450, wR_2 = 0.1043
Final R indexes [all data]	R_1 = 0.0483, wR_2 = 0.0874	R_1 = 0.0642, wR_2 = 0.1692	R_1 = 0.0565, wR_2 = 0.1084
Largest diff. peak/hole / e Å^{-3}	2.46/-0.77	3.54/-1.90	1.04/-0.41

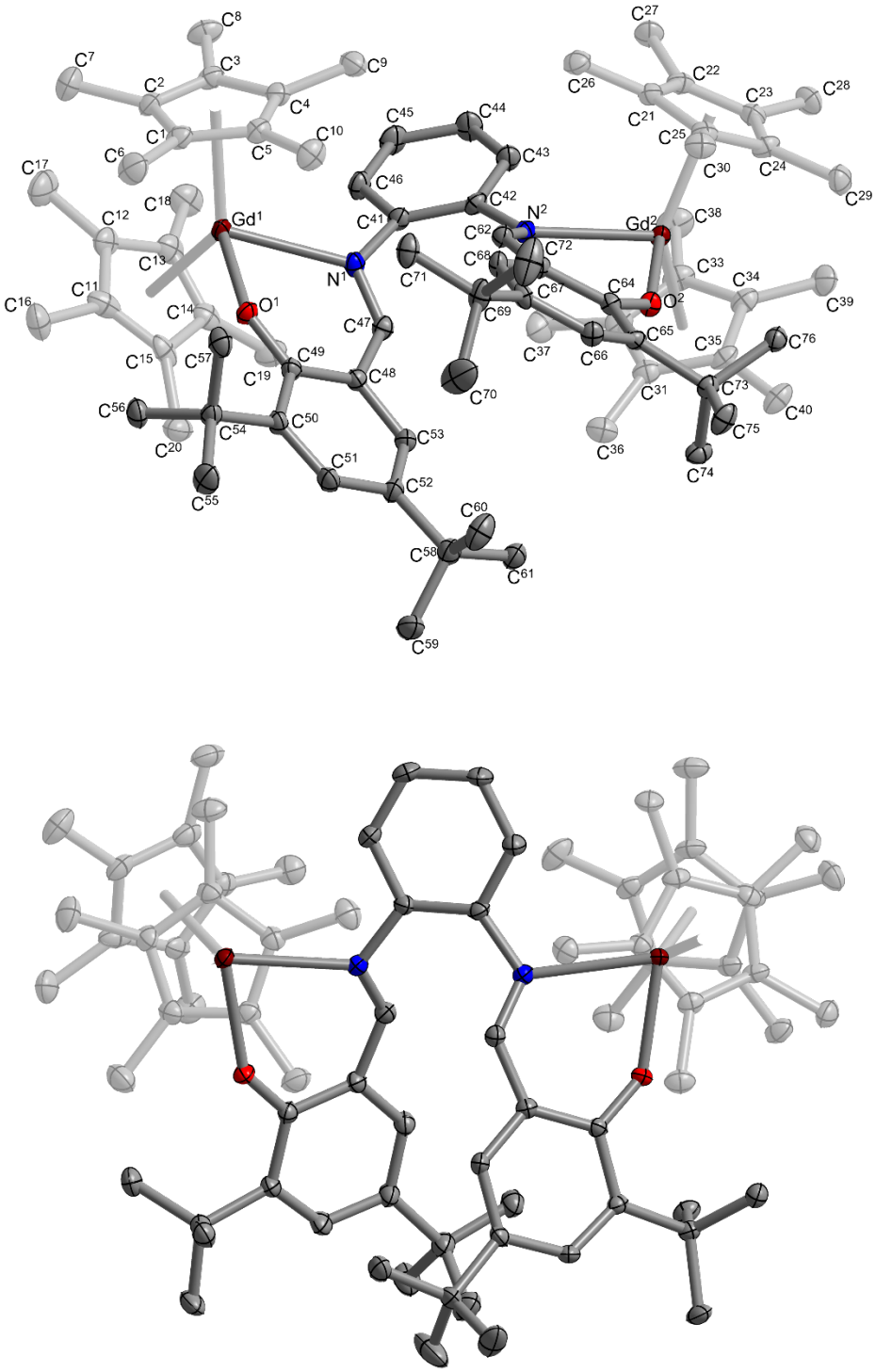

Fig. S1. Structure of $(Cp^*_2Gd)_2(\mu\text{-}^{tBu}salophen)$, **1**, with thermal ellipsoids drawn at 50% probability level. (Top) Front perspective of **1**, with corresponding atom labels. (Bottom) Top perspective of **1**. Maroon, red, blue, and grey ellipsoids represent Gd, O, N, and C atoms, respectively. $(Cp^*)^-$ ligands have been faded for clarity. Hydrogen atoms, and solvent molecules in the crystal lattice, have been omitted for clarity.

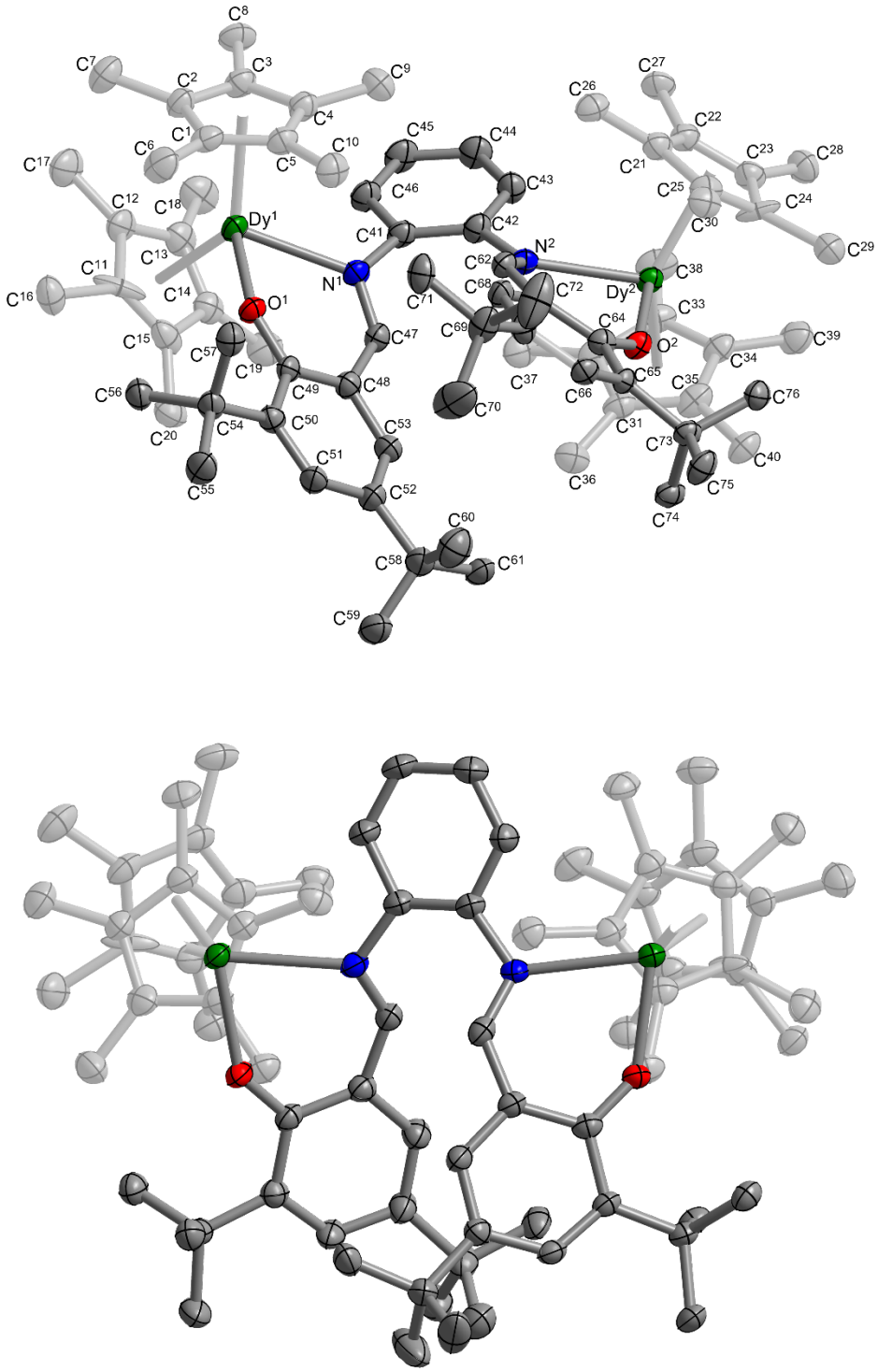

Fig. S2. Structure of $(Cp^*_2Dy)_2(\mu\text{-}^{tBu}salophen)$, **2**, with thermal ellipsoids drawn at 50% probability level. (Top) Top perspective of **2**, with corresponding atom labels. (Bottom) Front perspective of **2**. Green, red, blue, and grey ellipsoids represent Dy, O, N, and C atoms, respectively. $(Cp^*)^-$ ligands have been faded for clarity. Hydrogen atoms, and solvent molecules in the crystal lattice, have been omitted for clarity.

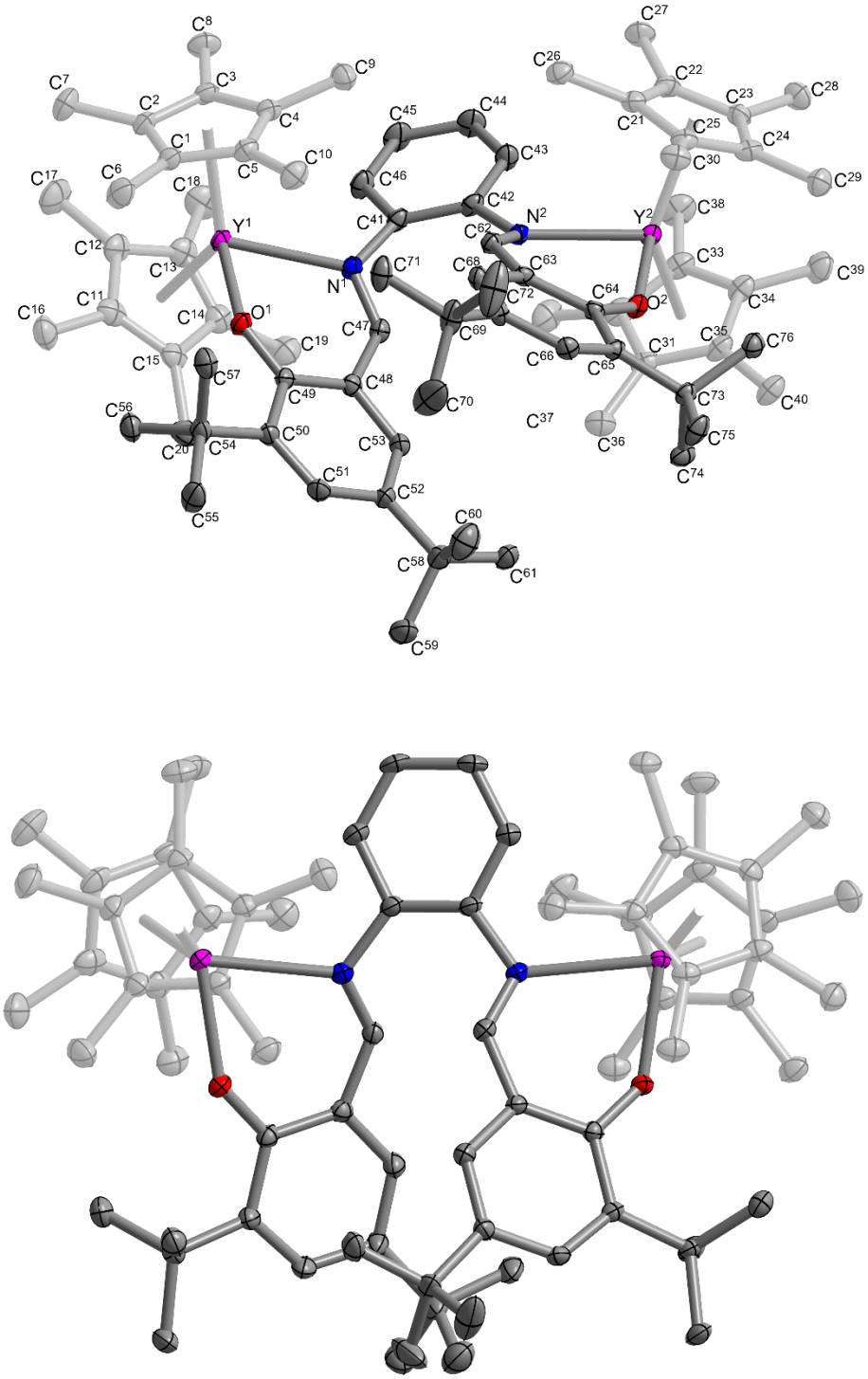

Fig. S3. Structure of $(Cp^*_2Y)_2(\mu\text{-}^{t\mathrm{Bu}}\text{salophen})$, **3**, with thermal ellipsoids drawn at 50% probability level. (Top) Top perspective of **3**, with corresponding atom labels. (Bottom) Front perspective of **3**. Pink, red, blue, and grey ellipsoids represent Y, O, N, and C atoms, respectively. $(Cp^*)^-$ ligands have been faded for clarity. Hydrogen atoms, and solvent molecules in the crystal lattice, have been omitted for clarity.

2 NMR Spectroscopy

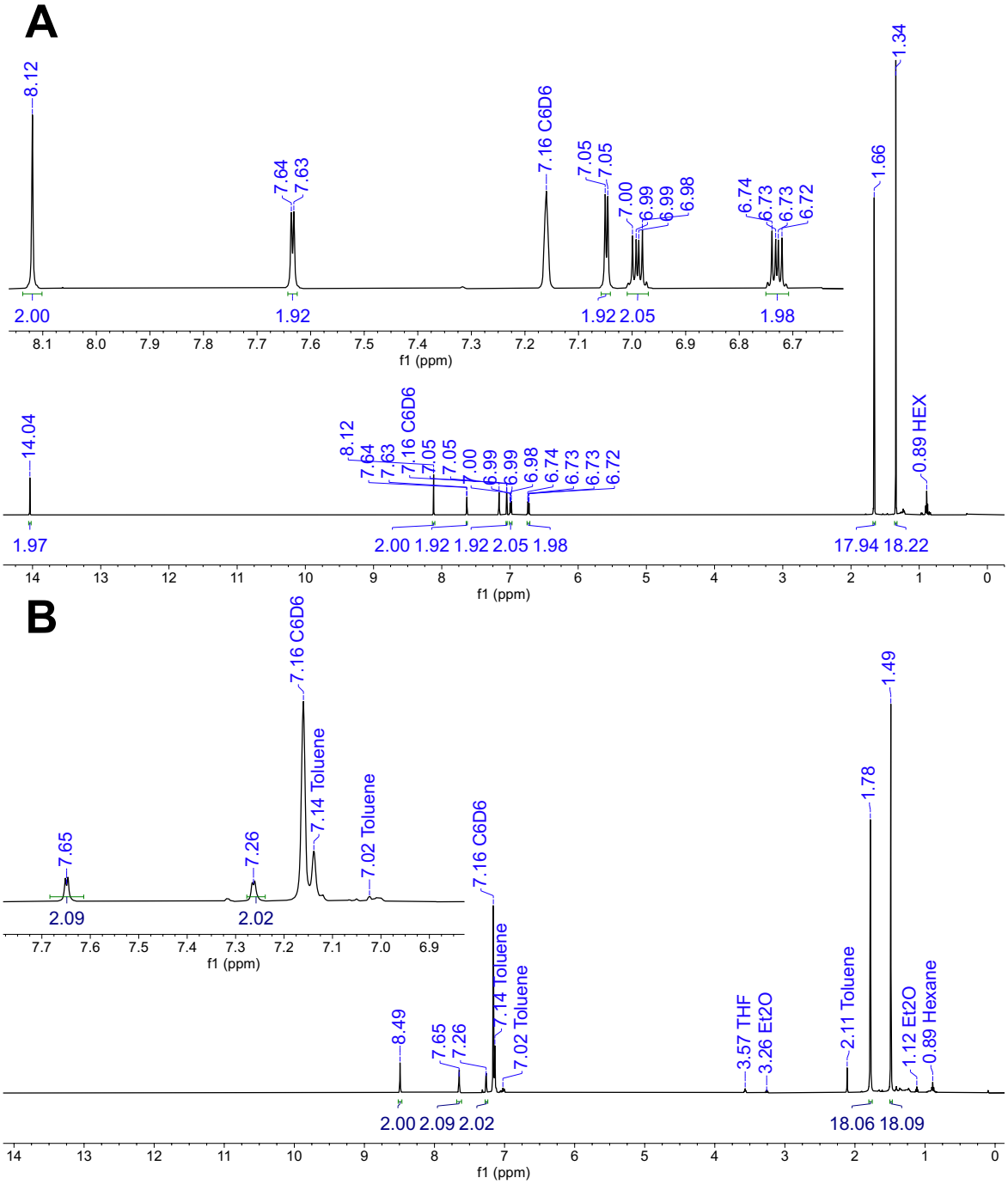

Fig. S4. (**A**) ^{1}H NMR (500 MHz, C_6D_6, 25 °C) spectrum of $H_2{}^{t\mathrm{Bu}}$salophen. δ (ppm): 14.04 (s, 2H, (C_6H_2)-O*H*), 8.12 (s, 2H, N=C*H*), 7.63 (d, $^4J_{\mathrm{H-H}}$ = 2.4 Hz, 2H, *p*-*H* (C_6H_2)), 7.05 (d, $^4J_{\mathrm{H-H}}$ = 2.4 Hz, 2H, *o*-*H* (C_6H_2), 6.99 (dd, $^3J_{\mathrm{H-H}}$ = 5.9, 3.4 Hz, 2H, *m*-C*H* (C_6H_4)), 6.73 (dd, $^3J_{\mathrm{H-H}}$ = 5.9, 3.4 Hz, 2H, *o*-C*H* (C_6H_4)), 1.66 (s, 18H, C*Me*$_3$), 1.34 (s, 18H, C*Me*$_3$). (**B**) ^{1}H NMR (500 MHz, C_6D_6, 25 °C) spectrum of $K_2{}^{t\mathrm{Bu}}$salophen. δ (ppm): 8.49 (s, 2H, N=C*H*), 7.65 (d, $^4J_{\mathrm{H-H}}$ = 2.8 Hz, 2H, *p*-C*H* (C_6H_2)), 7.26 (d, $^4J_{\mathrm{H-H}}$ = 2.8 Hz, 2H, *o*-C*H* (C_6H_4)), 1.78 (s, 18H, C*Me*$_3$), 1.49 (s, 18H, C*Me*$_3$). The ^{1}H NMR peaks of the *m*-C*H* (C_6H_4) and *o*-C*H* (C_6H_4) protons overlay with the solvent, and thus, are not assigned.

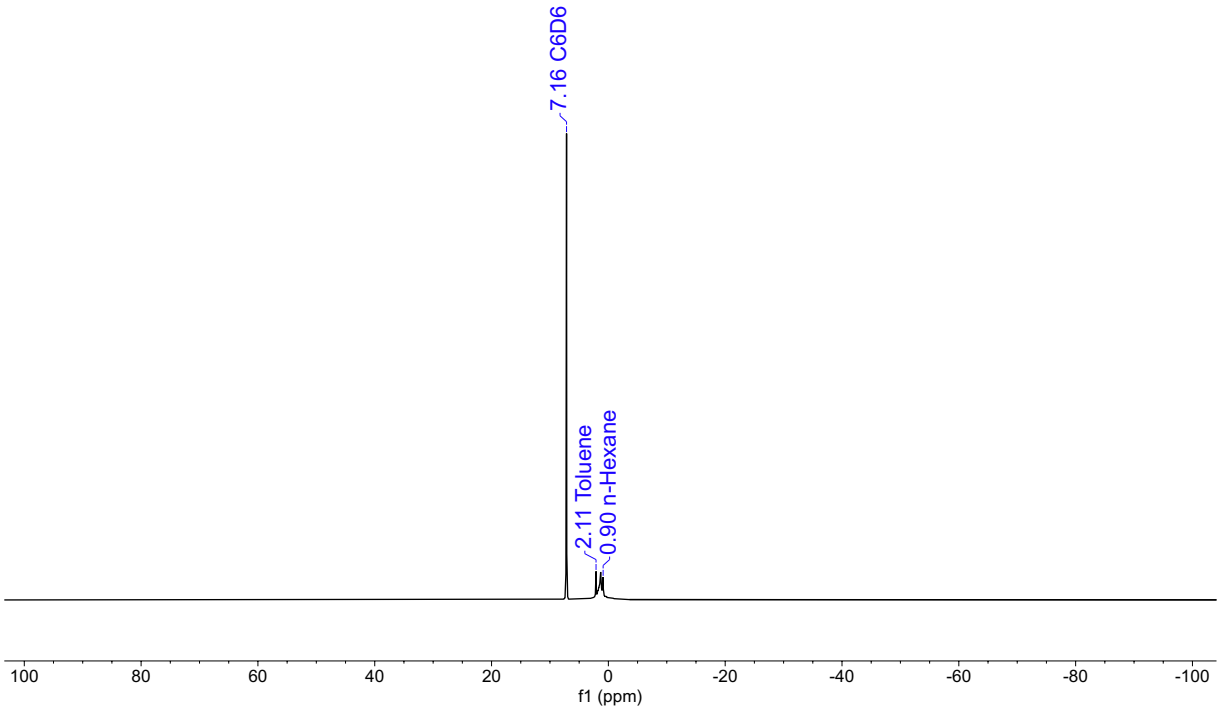

Fig. S5. ^{1}H NMR (500 MHz, C_6D_6, 25 °C) spectrum of $(Cp^*_2Gd)_2(\mu\text{-}^{t\mathrm{Bu}}\text{salophen})$, **1**. Due to the paramagnetic nature of **1**, no signals were observed in the ^{1}H NMR spectrum.

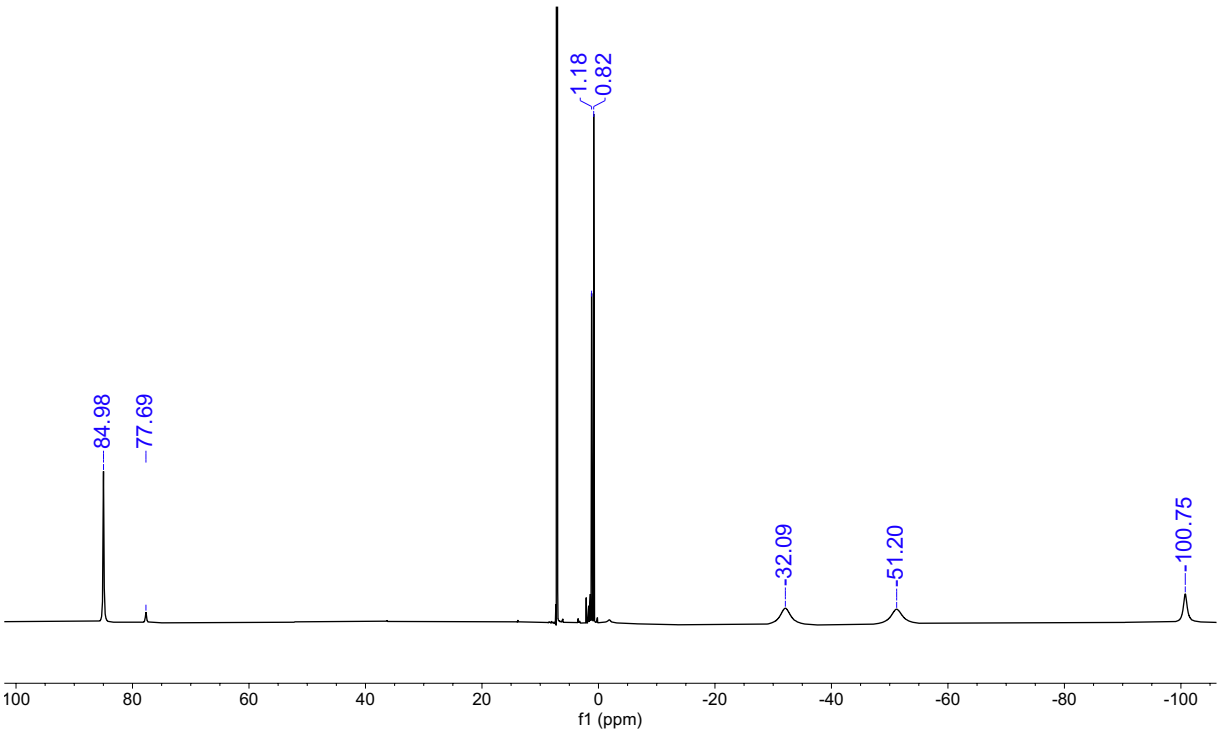

Fig. S6. ^{1}H NMR (500 MHz, C_6D_6, 25 °C) spectrum of $(Cp^*_2Dy)_2(\mu\text{-}^{t\mathrm{Bu}}\text{salophen})$, **2**. δ (ppm): 84.98, 77.69, 7.32, 7.00, 1.18, 0.82, −32.09 (br), −51.20 (br), −100.75.

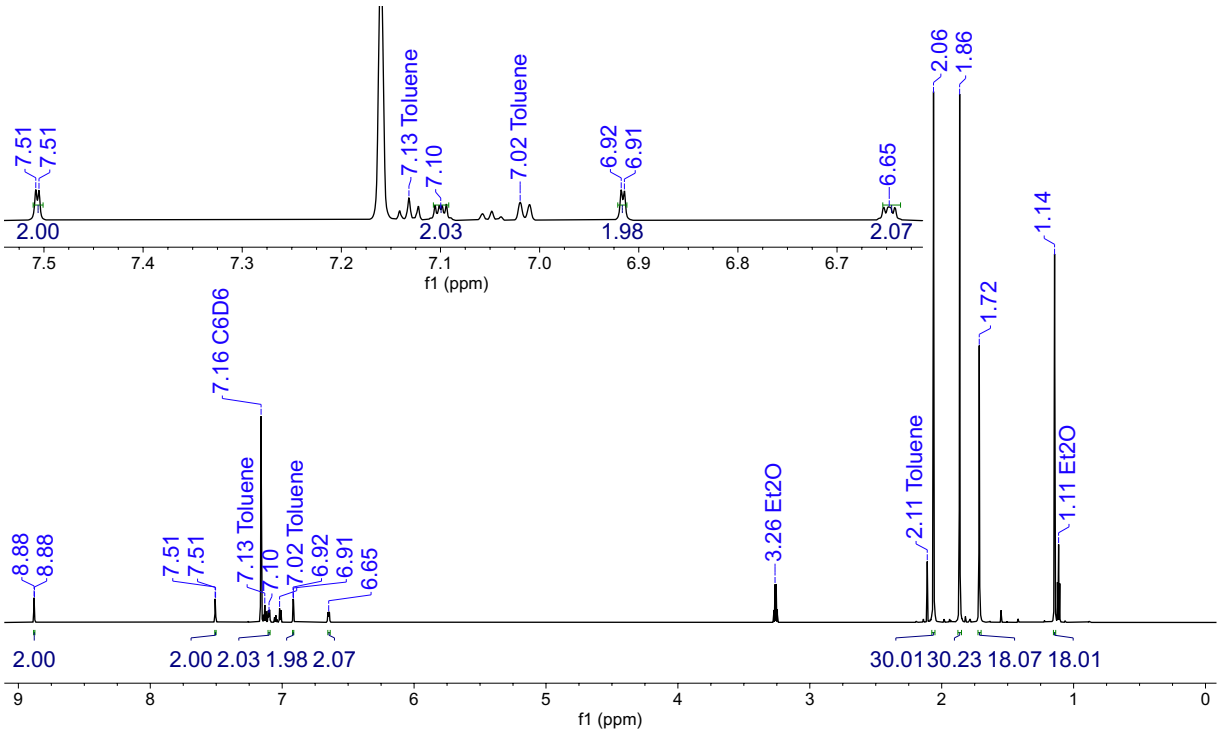

Fig. S7. ^{1}H NMR (800 MHz, C_6D_6, 25 °C) spectrum of $(Cp^*_2Y)_2(\mu\text{-}^{t\mathrm{Bu}}\text{salophen})$, **3**. δ (ppm): 8.88 (d, $^{3}J_{Y-H}$ = 2.2 Hz, 2H, N=C*H*), 7.51 (d, $^{4}J_{H-H}$ = 2.6 Hz, 2H, *p*-C*H* (C_6H_2)), 7.10 (dd, $^{3}J_{H-H}$ = 5.8, 3.4 Hz, 2H, *m*-C*H* (C_6H_4)), 6.92 (d, $^{4}J_{H-H}$ = 2.6 Hz, 2H, *o*-C*H* (C_6H_2)), 6.65 (dd, $^{3}J_{H-H}$ = 5.8, 3.4 Hz, 2H, *o*-C*H* (C_6H_4)), 2.06 (s, 30H, C_5Me_5), 1.86 (s, 30H, C_5Me_5), 1.72 (s, 18H, CMe_3), 1.14 (s, 18H, CMe_3).

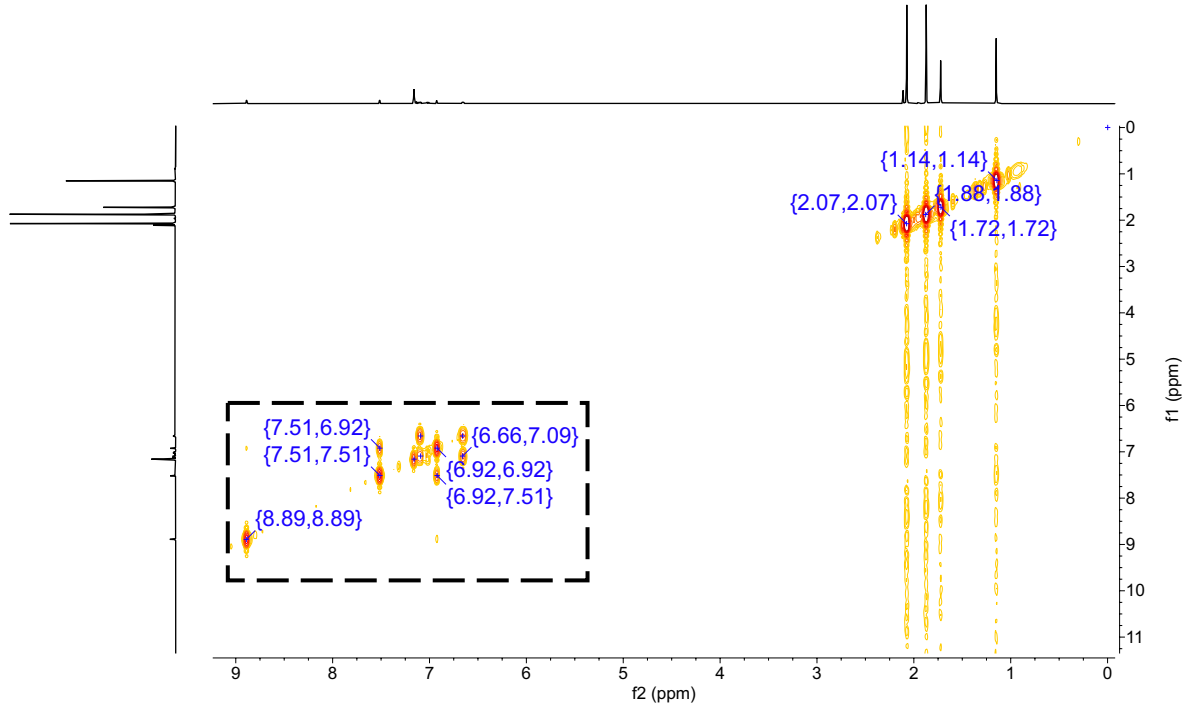

Fig. S8. ^{1}H–^{1}H COSY (500 MHz, C_6D_6, 25 °C) spectrum of $(Cp^*_2Y)_2(\mu\text{-}^{t\mathrm{Bu}}\text{salophen})$, **3**.

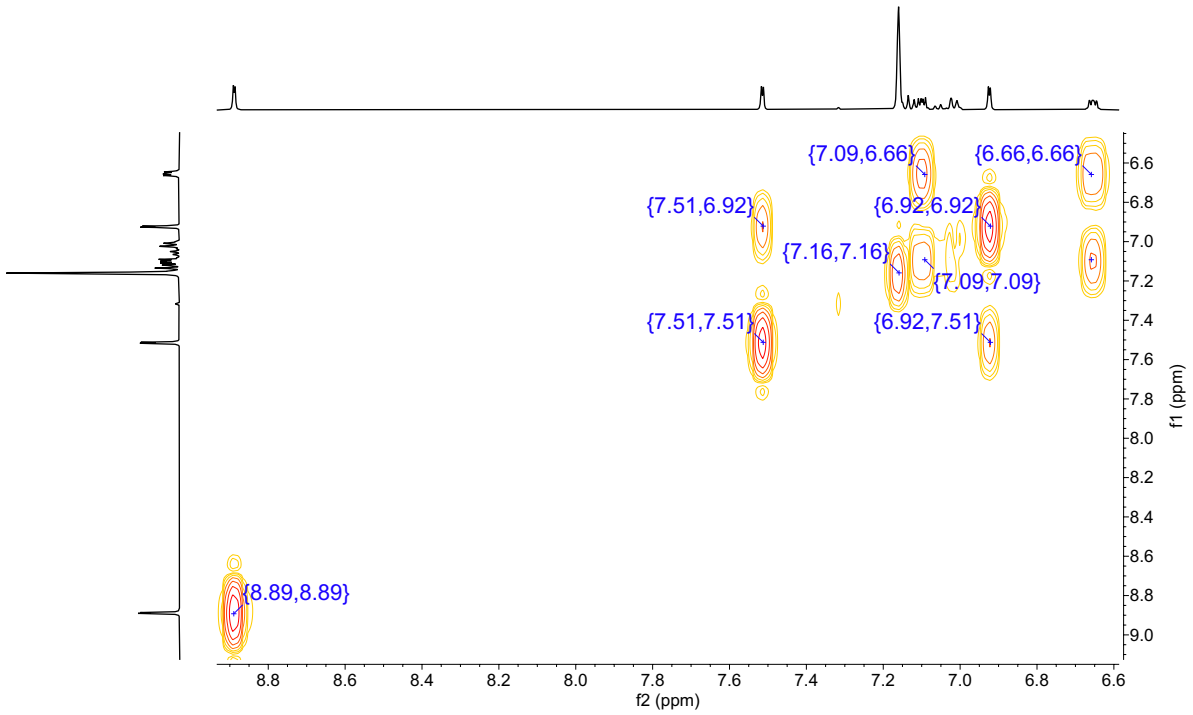

Fig. S9. Enlarged ^{1}H–^{1}H COSY (500 MHz, C_6D_6, 25 °C) spectrum of $(Cp^*_2Y)_2(\mu\text{-}^{t\mathrm{Bu}}\text{salophen})$, **3**.

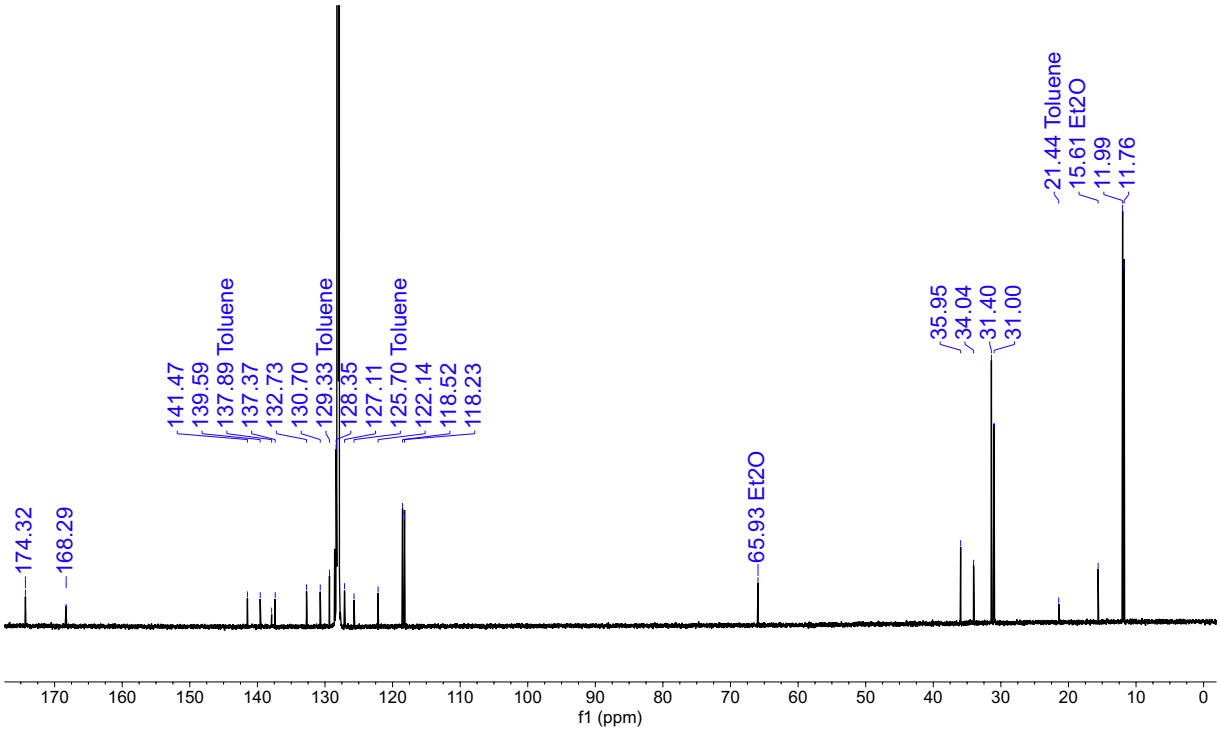

Fig. S10. ^{13}C NMR (800 MHz, C_6D_6, 25 °C) spectrum of $(Cp^*_2Y)_2(\mu\text{-}^{t\mathrm{Bu}}\text{salophen})$, **3**. δ (ppm): 174.32 (N=*C*H), 168.29 ((C_6H_2)*C*-O), 141.47 ((C_6H_4)*C*-N), 139.59 ((C_6H_2)*C*-CMe_3), 137.37 ((C_6H_2)*C*-CMe_3), 132.73 (*p*-*C*H (C_6H_2)), 130.70 (*o*-*C*H (C_6H_2)), 128.35 (*m*-*C*H (C_6H_4)), 127.11 (*o*-*C*H (C_6H_4)), 122.14 (C_6H_2)*C*-CH), 118.52 (C_5Me_5), 118.23 (C_5Me_5), 35.95 (CMe_3), 34.04 (CMe_3), 31.40 (C*Me*$_3$), 31.00 (C*Me*$_3$), 11.99 (C_5*Me*$_5$), 11.76 (C_5*Me*$_5$).

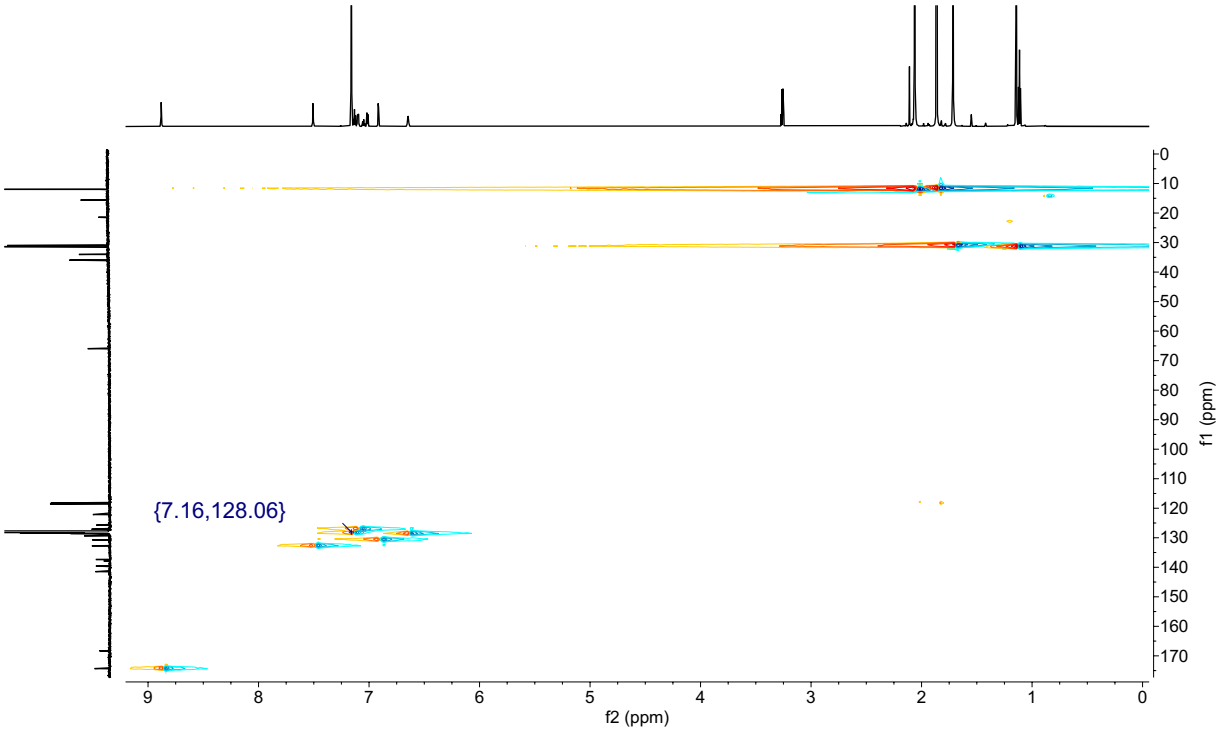

Fig. S11. $^{1}H–^{13}C$ HSQC (500 MHz, C_6D_6, 25 °C) spectrum of $(Cp^*_2Y)_2(\mu\text{-}^{tBu}salophen)$, **3**.

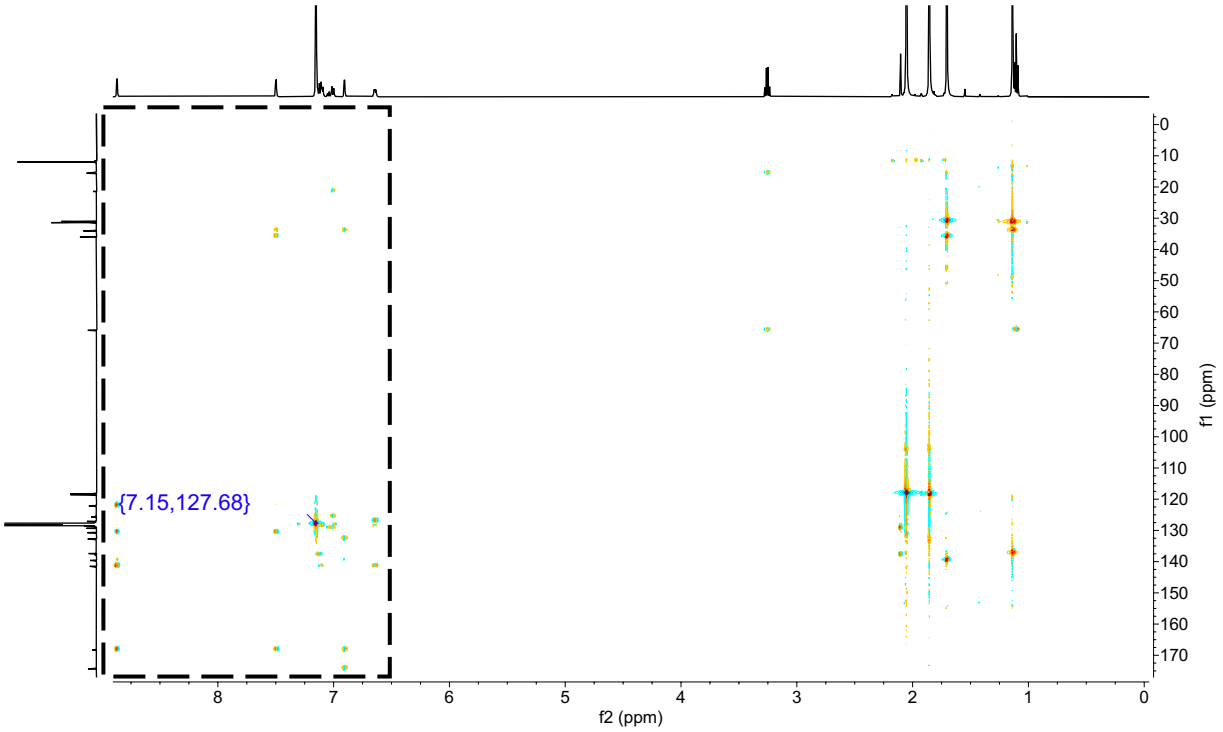

Fig. S12. $^{1}H–^{13}C$ HMBC (500 MHz, C_6D_6, 25° C) spectrum of $(Cp^*_2Y)_2(\mu\text{-}^{tBu}salophen)$, **3**.

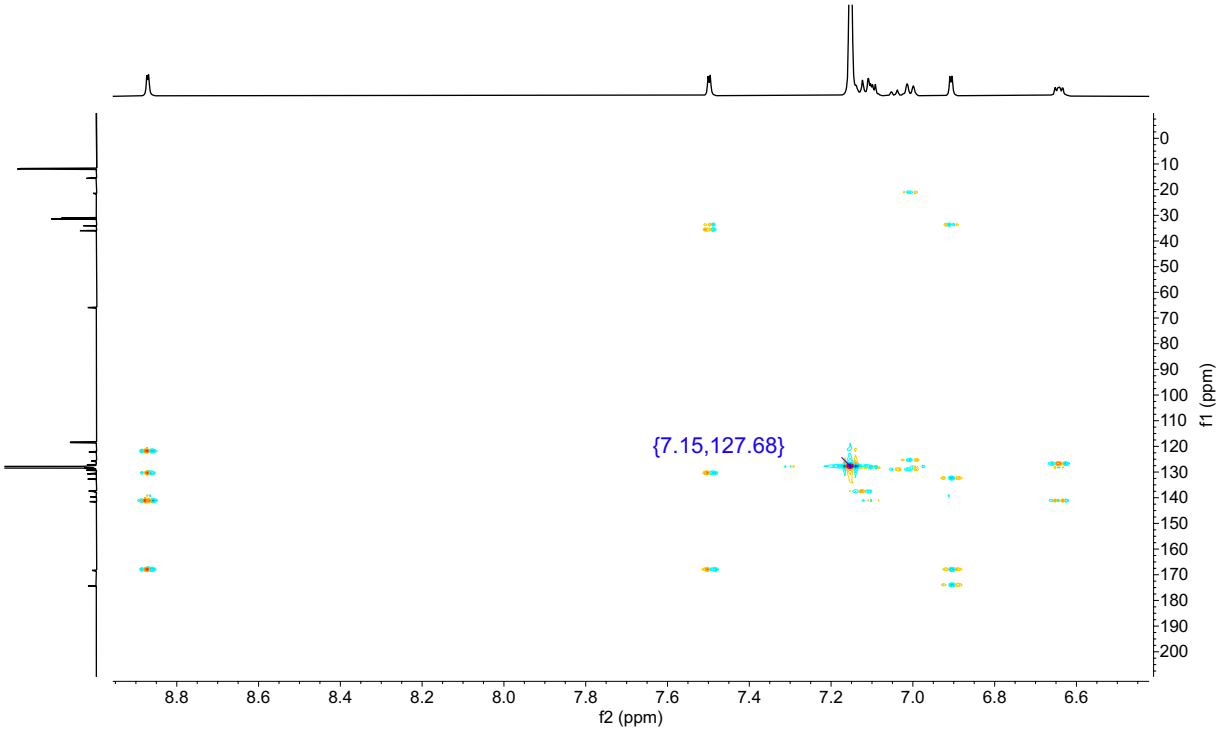

Fig. S13. Enlarged $^{1}H–^{13}C$ HMBC (500 MHz, C_6D_6, 25 °C) spectrum of $(Cp^*_2Y)_2(\mu\text{-}^{tBu}salophen)$, **3**.

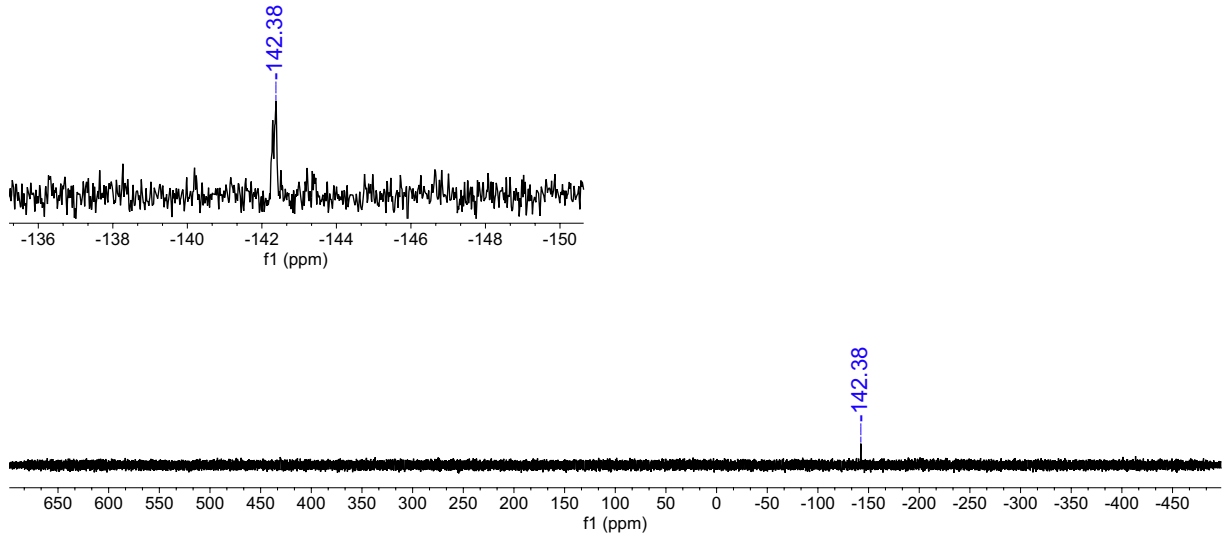

Fig. S14. Proton-coupled ^{89}Y NMR (20 mmol, 500 MHz, C_6D_6, 25 °C) spectrum of $(Cp^*_2Y)_2$(μ-^{t}Bu salophen), **3**, measured from 700 ppm to –500 ppm in the absence of an external reference. δ (ppm): −142.38.

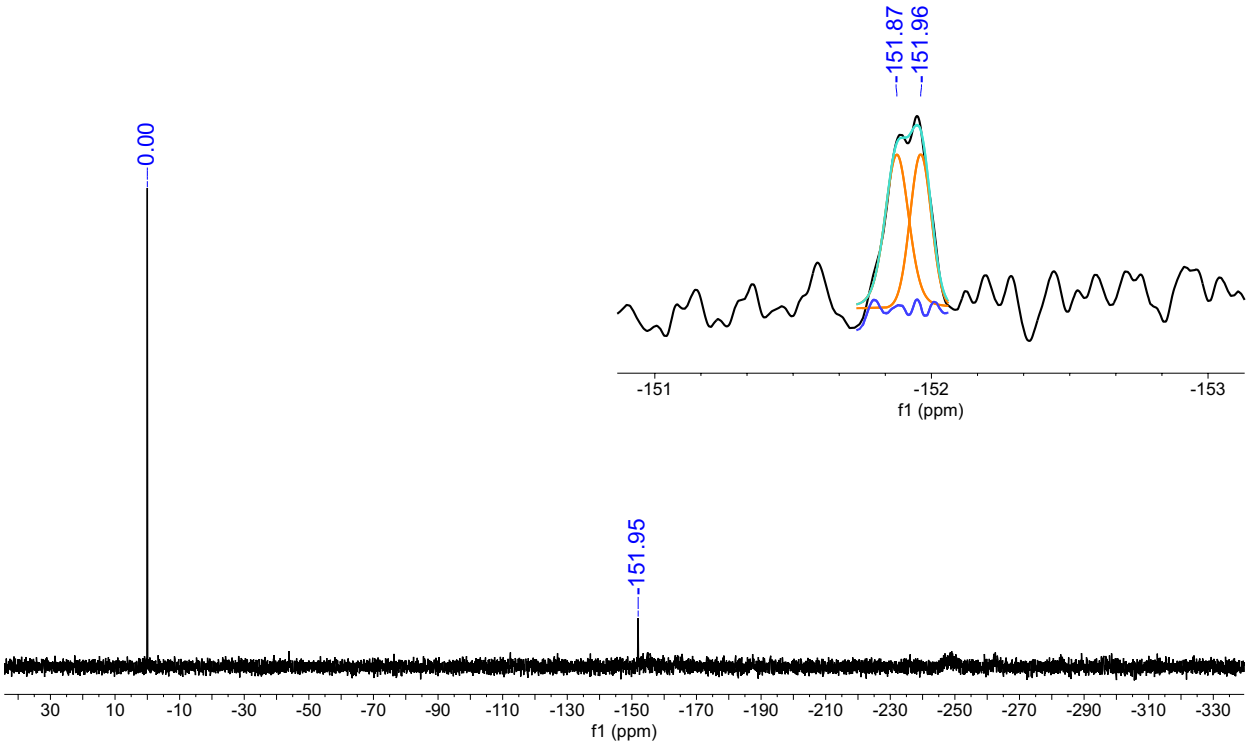

Fig. S15. Proton-coupled ^{89}Y NMR (20 mmol, 500 MHz, C_6D_6, 25 °C) spectrum of $(Cp^*_2Y)_2$(μ-^{t}Bu salophen), **3**, measured from 50 ppm to –350 ppm. Inset of ^{89}Y NMR spectrum from –151 to –153 ppm. δ (ppm): −151.92 (d, $^3J_{Y-H}$ = 2.2 Hz, N=C*H*). The peak was deconvoluted through a Lorentzian-Gaussian function as implemented in MestReNova V 14.1.1. The turquoise, orange, and blue lines denote the fitted doublet peak, the fitted sum, and residuals, respectively. ^{89}Y NMR signal is referenced to a 3 M solution of YCl_3 in D_2O.

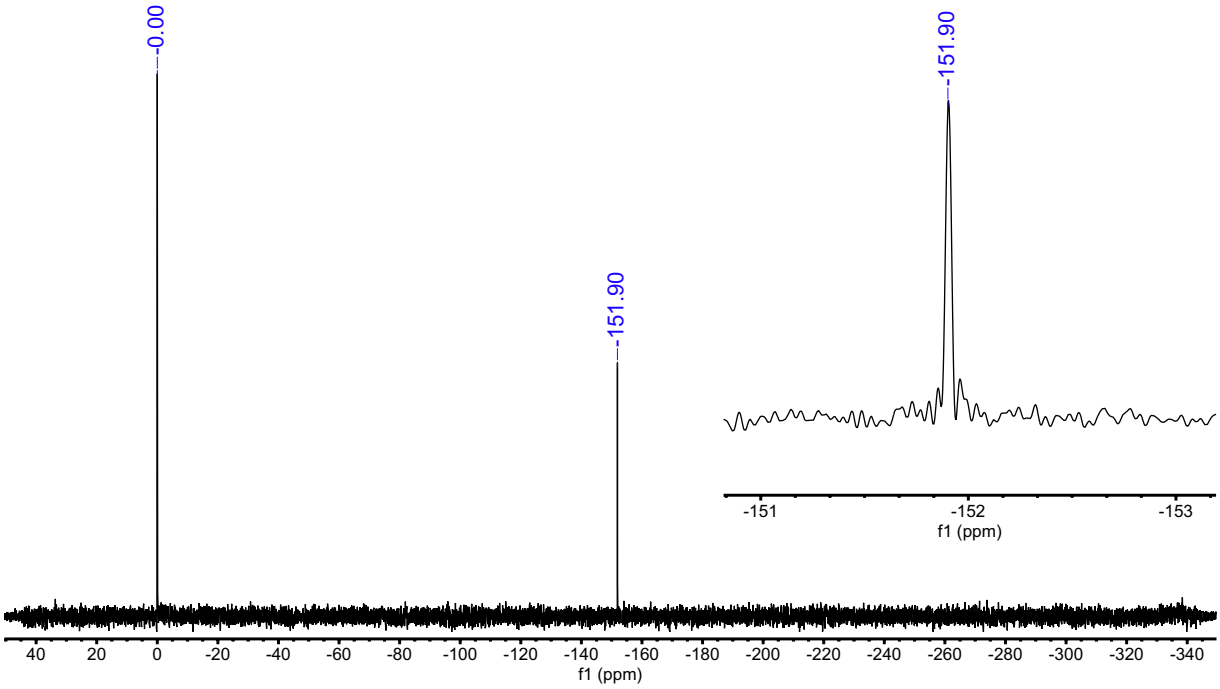

S16. Proton-decoupled ^{89}Y NMR (^{89}Y-{^{1}H}) (20 mmol, 500 MHz, C_6D_6, 25 °C) spectrum of $(Cp^*_2Y)_2(\mu\text{-}^{t\text{Bu}}\text{salophen})$, **3**, measured from 50 ppm to –350 ppm. Inset of ^{89}Y-{^{1}H} NMR spectrum from –151 to –153 ppm. δ (ppm): –151.90 (s). ^{89}Y NMR signal is referenced to a 3 M solution of YCl_3 in D_2O.

3 IR Spectroscopy

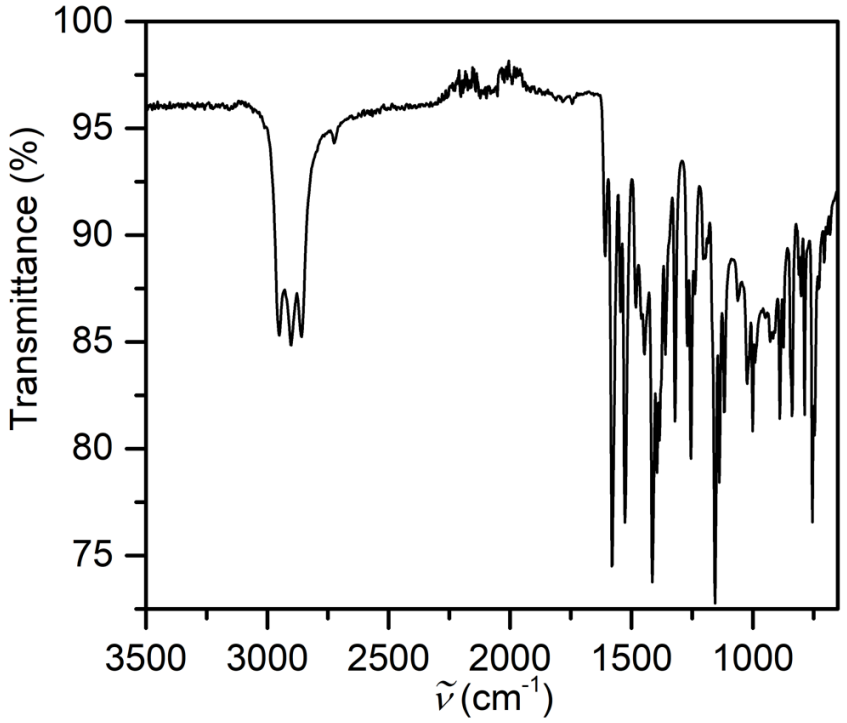

Fig. S17. FTIR spectrum on crushed crystalline solids of $(Cp^*_2Gd)_2(\mu\text{-}^{t\mathrm{Bu}}\text{salophen})$, **1**, measured in a nitrogen-filled glovebox.

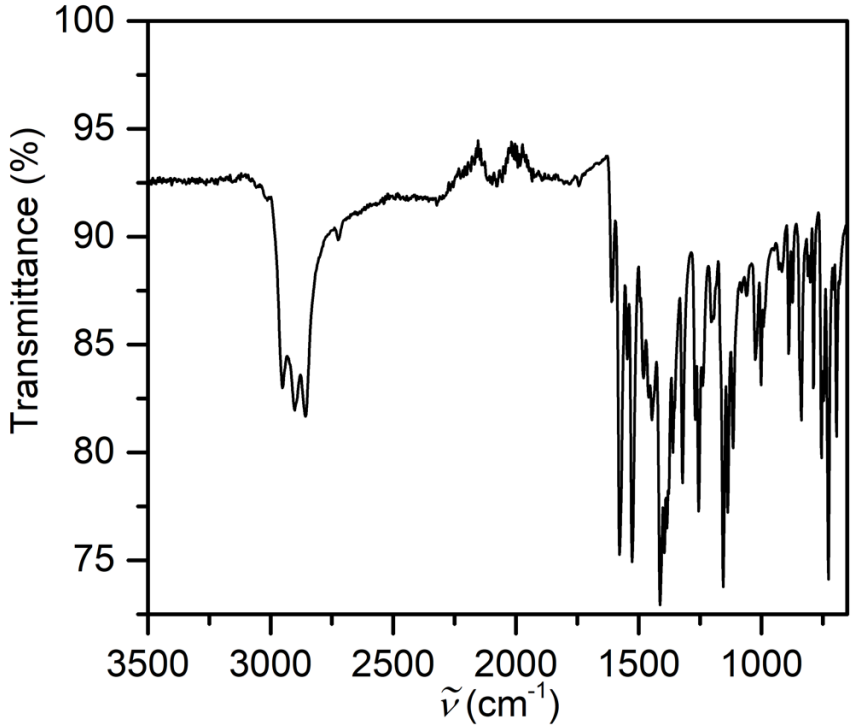

Fig. S18. FTIR spectrum on crushed crystalline solids of $(Cp^*_2Dy)_2(\mu\text{-}^{t\mathrm{Bu}}\text{salophen})$, **2**, measured in a nitrogen-filled glovebox.

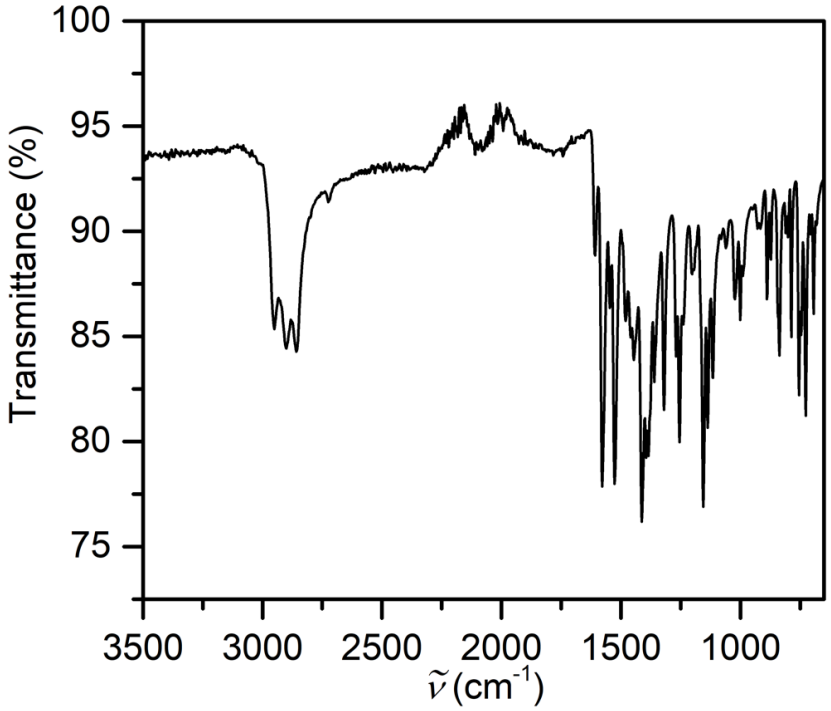

Fig. S19. FTIR spectrum on crushed crystalline solids of $(Cp^*_2Y)_2(\mu\text{-}^{tBu}salophen)$, **3**, measured in a nitrogen-filled glovebox.

4 Magnetic Measurements

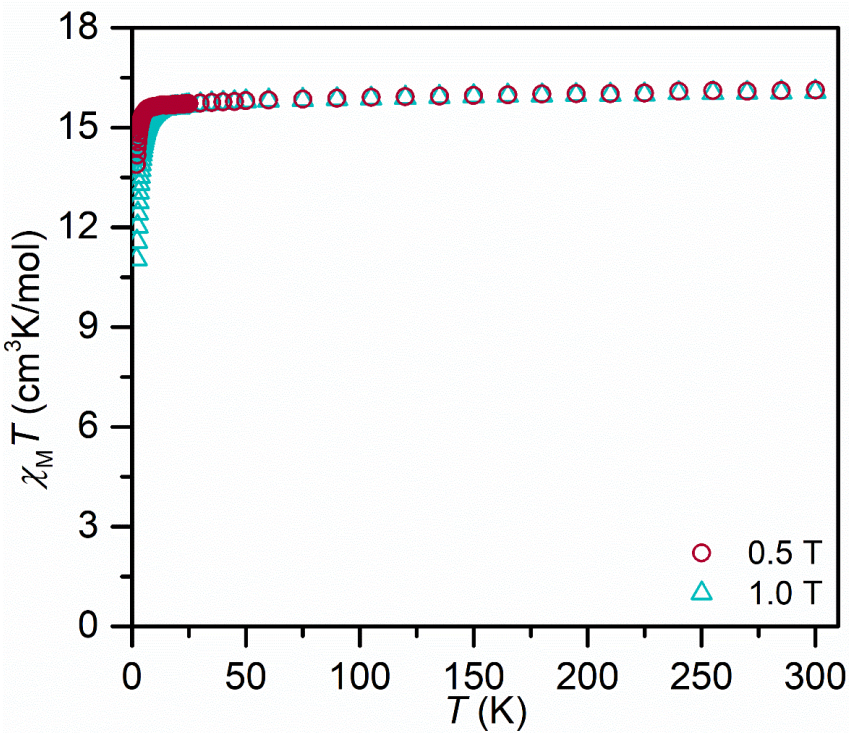

Fig. S20. Plots of $\chi_M T$ vs. T for (Cp*$_2$Gd)$_2$(μ-$^{t\mathrm{Bu}}$salophen), **1**, between 2 and 300 K under an applied dc field of 0.5 T (red circles), and 1.0 T (cyan triangles).

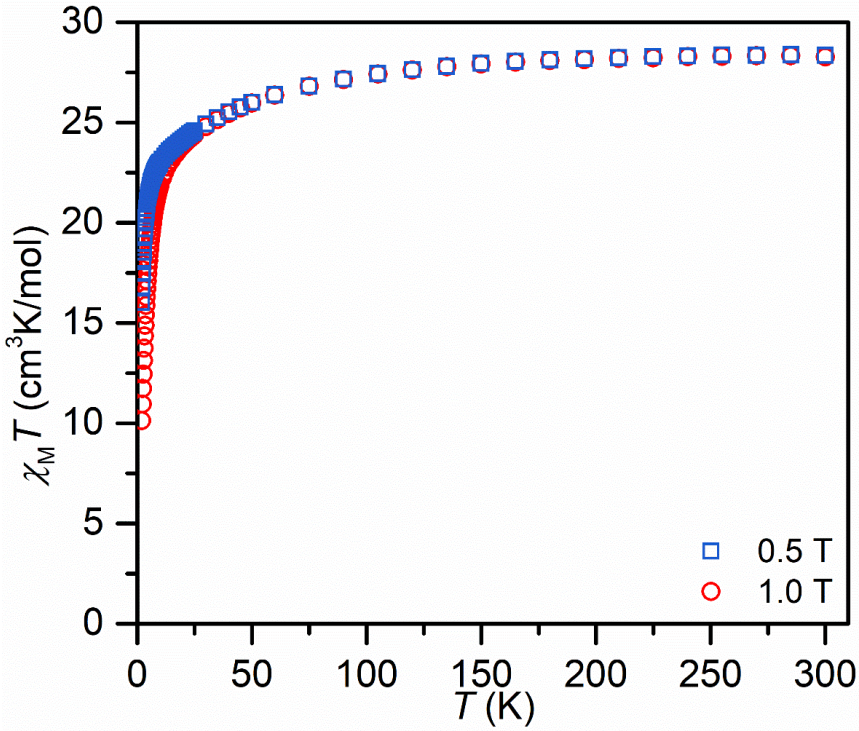

Fig. S21. Plots of $\chi_M T$ vs. T for (Cp*$_2$Dy)$_2$(μ-$^{t\mathrm{Bu}}$salophen), **2**, between 2 and 300 K under an applied dc field of 0.5 T (blue squares), and 1.0 T (red circles).

Table S2. Magnetic exchange coupling constant, *J*, *g* values, and residuals from fitting $\chi_M T$ vs. *T* for **1** between 1.8 and 300 K under an applied dc field of 0.5 and 1.0 T with PHI.[1]

	g	***J* (cm^{-1})**	***zJ'* (cm^{-1})**	***Residuals***
0.5 T	2.0542	-	-	66.4176
0.5 T	1.9923	0.0295±0.0029	-	18.7860
0.5 T	1.9923	-	0.0105±0.0002	4.8147
0.5 T	1.9947	−0.049±0.0037	0.0178±0.001	3.3652
1.0 T	2.0269	-	-	4.8486
1.0 T	2.0077	−0.0053±0.0004	-	0.4621
1.0 T	2.0100	-	0.0030±0.0001	0.5149
1.0 T	2.0066	−0.0823±0.0032	0.0215±0.0013	1.0191

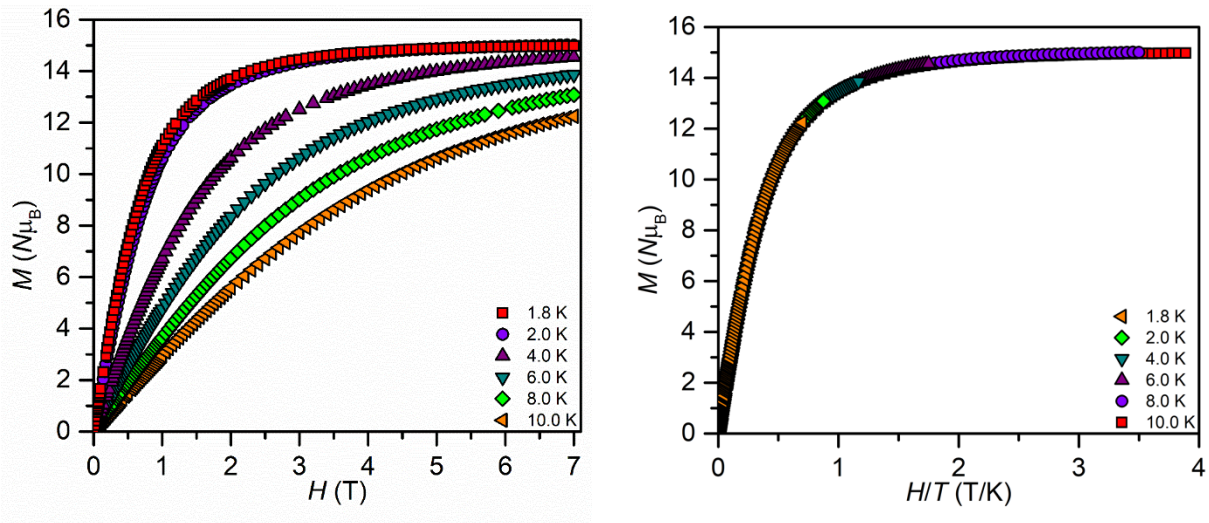

Fig. S22. Field-dependent magnetization (left) and reduced magnetization (right) data for $(Cp^*_2Gd)_2(\mu\text{-}^{tBu}salophen)$, **1**, between 0 and 7 T from 1.8 to 10 K.

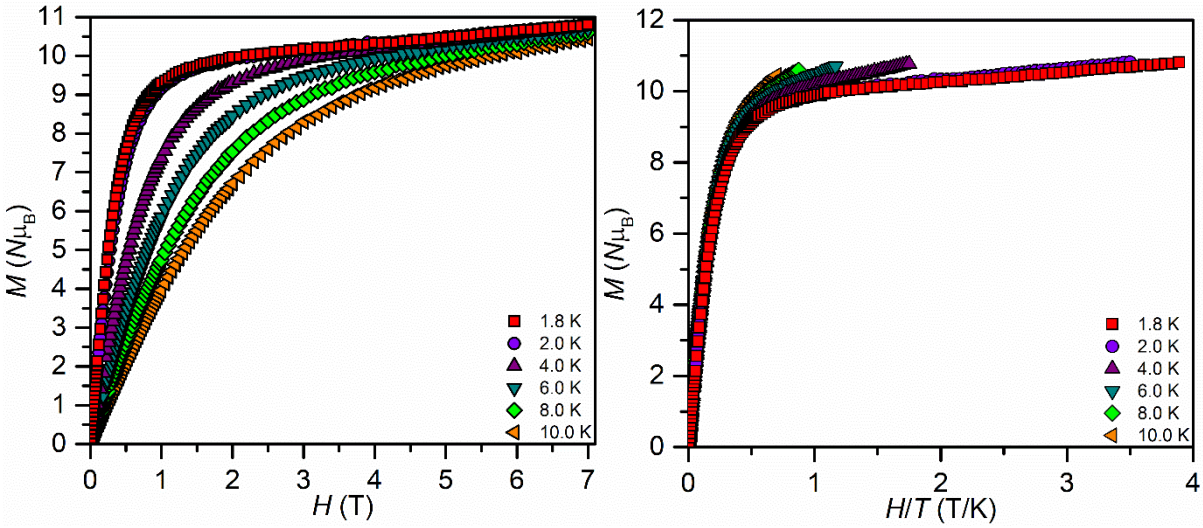

Fig. S23. Field-dependent magnetization (left) and reduced magnetization (right) data for $(Cp^*_2Dy)_2(\mu\text{-}^{t\mathrm{Bu}}\text{salophen})$, **2**, between 0 and 7 T from 1.8 to 10 K.

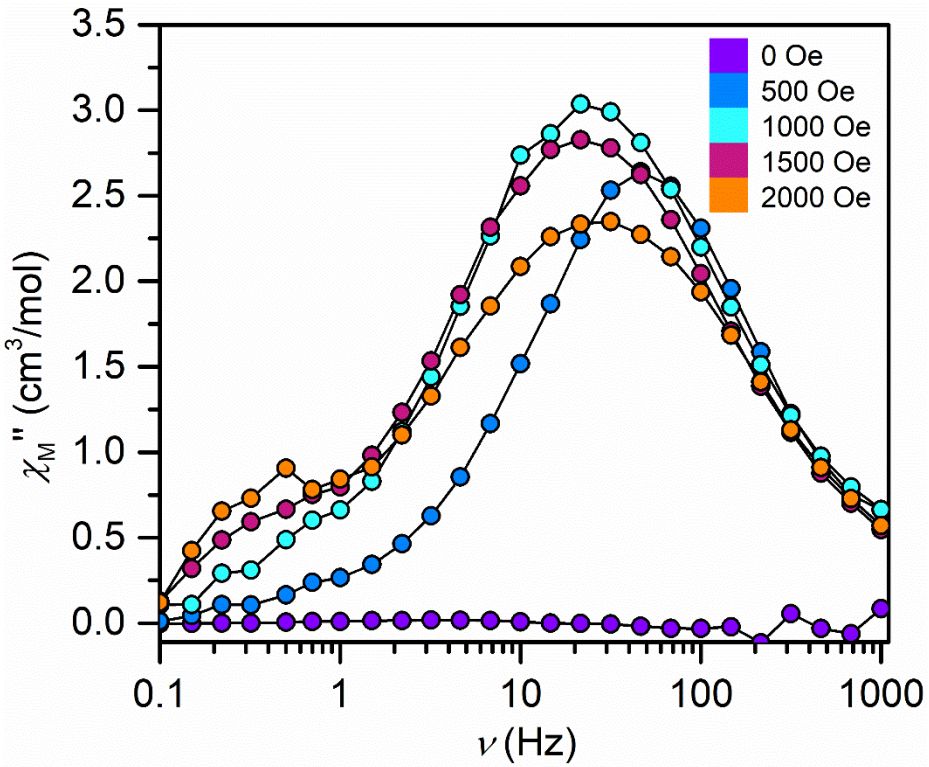

Fig. S24. Ac field scan at 2 K of $(Cp^*_2Dy)_2(\mu\text{-}^{t\mathrm{Bu}}\text{salophen})$, **2**, collected from 0 Oe to 2000 Oe in 500 Oe increments. The solid lines represent guides for the eye.

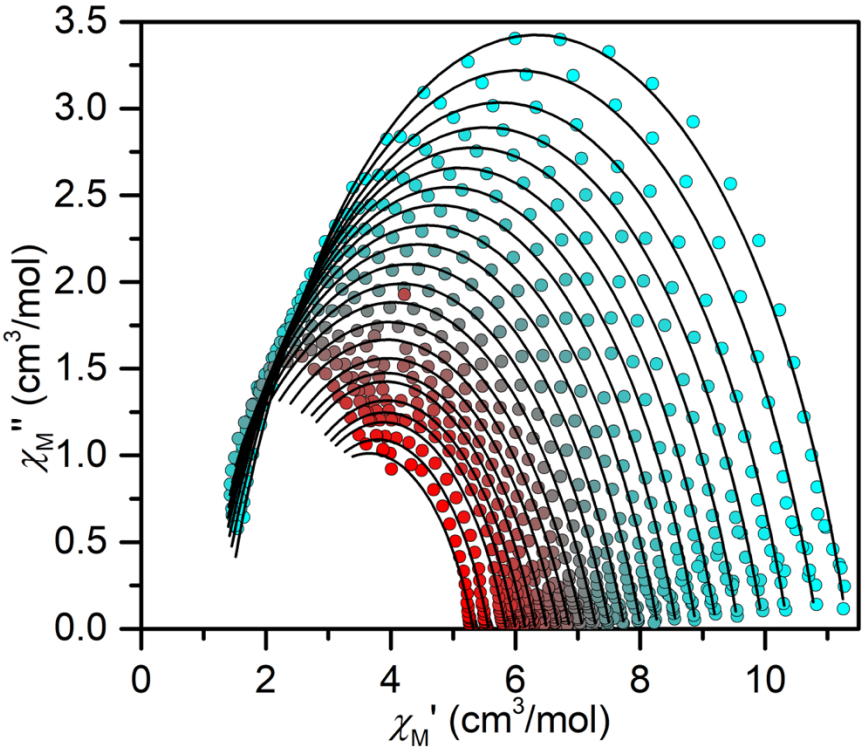

Fig. S25. Cole-Cole plots for ac magnetic susceptibility collected from 1.8 to 4.2 K, under a 1000 Oe applied dc field for $(Cp^*_2Dy)_2(\mu\text{-}^{tBu}salophen)$, **2**. The solid lines represent fits to the data.

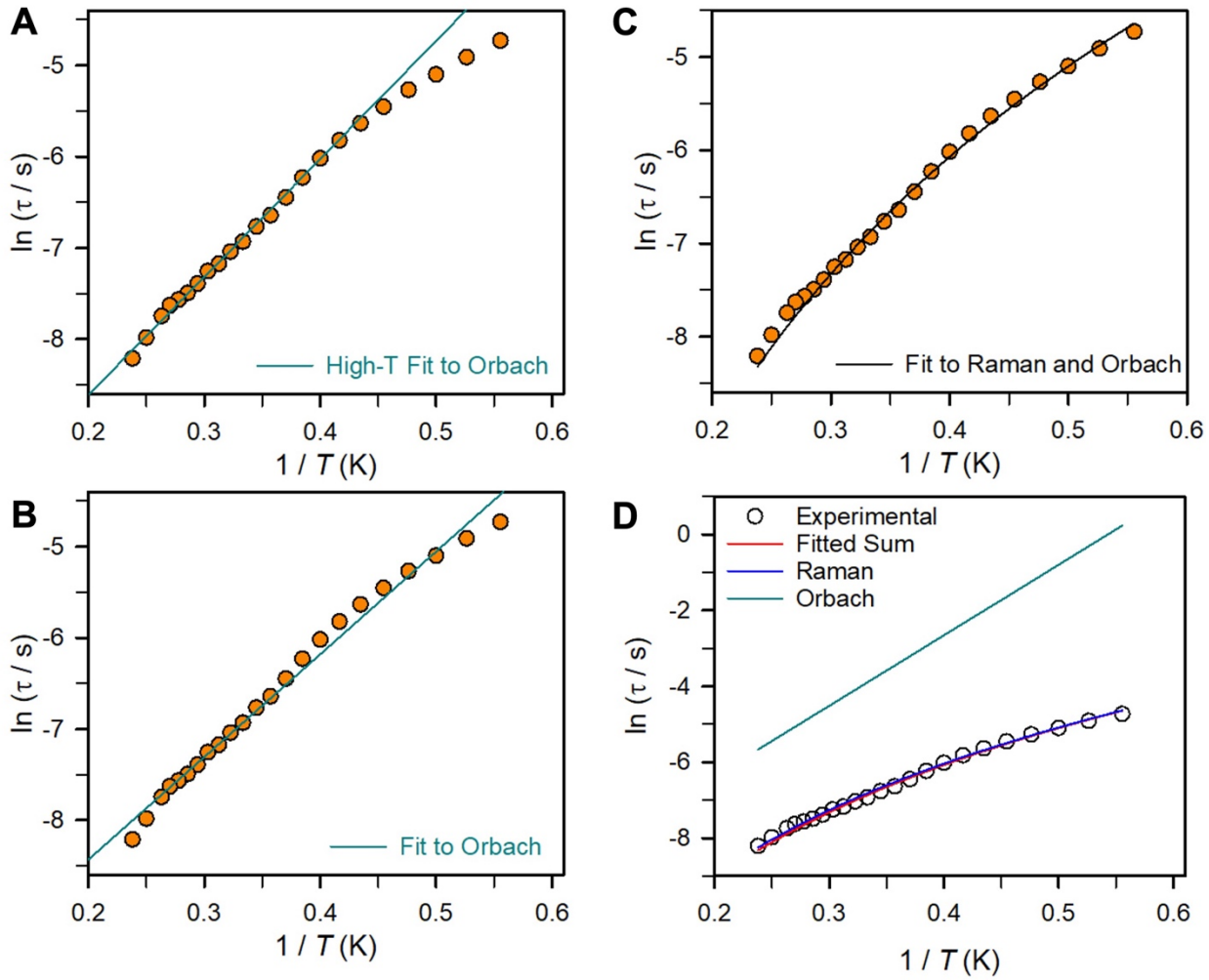

Fig. S26. Arrhenius plots of relaxation time data for $(Cp^*_2Dy)_2(\mu\text{-}^{t\mathrm{Bu}}\text{salophen})$, **2**. The orange circles represent the experimental data. The solid lines correspond to fits to data collected between 1.8 and 4.2 K. The solid cyan line in **A** represents a fit of the data between 3.3 and 4.2 K (High-T) to an Orbach process yielding a barrier to spin-reversal of U_{eff} = 8.9(4) cm^{-1} and a pre-exponential factor of τ_0 = 1.3(2)·10^{-5} s. Fitting the entire probed temperature range, **B**, solid cyan line, from 1.8 to 4.2 K afforded a similar barrier height and attempt time: U_{eff} = 7.8(2) cm^{-1} and τ_0 = 2.3(2)·10^{-5} s. The solid black line in **C** represents a fit to a Raman and Orbach relaxation process to give C = 8.39 s^{-1}K^{-n}, n = 4.27, and U_{eff} = 12.91(5) cm^{-1} and τ_0 = 4.2(1)·10^{-5} s. **D** arises from individual contributions of the Orbach (cyan line) and Raman (blue line) magnetic relaxation pathways to the Arrhenius plot of **2** at 1000 Oe.

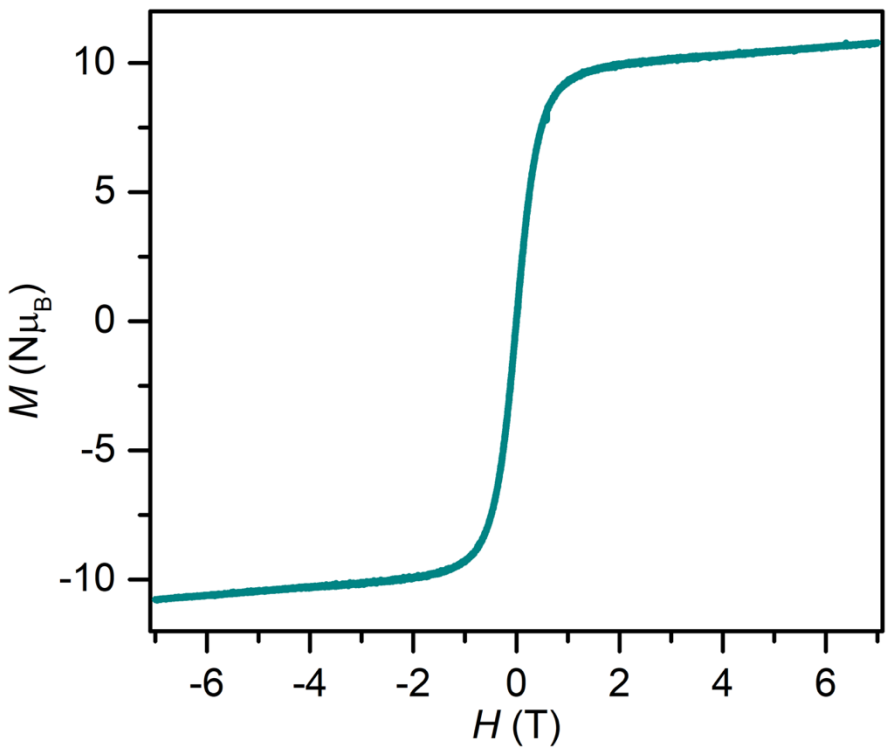

Fig. S27. Variable field magnetization (M) data for $(Cp^*_2Dy)_2(\mu\text{-}^{tBu}salophen)$, **2**, at 1.8 K and collected between -7 and +7 T at an average sweep rate of 100 Oe/s.

Table S3. Selected multinuclear Gd and Dy complexes containing diamagnetic bridging ligands for which exchange coupling constants were determined, either through direct measurements (Gd) or CASSCF calculations (Dy). *J* values are reported on the basis of the Hamiltonian $\widehat{H} = -2J\widehat{S}_A\widehat{S}_B$ with A and B representing the interactions of paramagnetic centers, metal ions and/or radical ligands. Abbreviations used in the formula are defined underneath the table.

Formula	*J* [cm^{-1}]	Notes	Ref
$\{(Me_3Si)_2N\}_2(THF)Ln]_2(\mu\text{-}\eta^2\text{:}\eta^2\text{-}N_2)$	–0.49		2
$[Cp^*_4Dy_2(\mu\text{-}BPh_4)][Al(OC(CF_3)_3)_4]$	0.0014	ac	3
$[\{Cp^*_2Dy(\mu\text{-}Me_3AlNEt_3)\}_2][Al\{OC(CF_3)_3\}_4]_2$	−0.21	a	4
$[\{Cp'_2Gd(\mu\text{-}SSiPh_3)\}_2]$	–0.105		5
$[Cp'_2Dy(THF)(\mu\text{-}Cl)]_2$	–1.90525	a	5
$[\{Cp'_2Dy(\mu\text{-}Cl)\}_2]$	–4.42025	a	5
$[Cp'_2Dy\{\mu\text{-}Sb(H)Mes\}]_3$	–0.121	b	6
$[(Cp'_2Dy)_3\{\mu\text{-}(SbMes)_3Sb\}]$	–0.150	b	6
$[(Cp^*_2Gd)_2(\mu\text{-ind})]$	–0.013(1)		7
$[\{K(THF)_3\}_2(Cp^*_2Ln)_2(\mu\text{-ind})]$	–0.018(1)		7
$[(Cp'_2Dy)\{\mu\text{-}As(H)Mes\}]_3$	–4.92 - –6.87	a	8
$[Li(THF)_4]_2[(Cp'_2Dy)_3(\mu_3\text{-}AsMes)_3Li]\bullet THF$	–6.61- –9.76	a	8
$[(Cp'_2Dy)\{\mu\text{-}SeMes\}]_3\bullet tol$	–4.76 - –5.02	a	8
$[(Cp'_2Dy)\{\mu\text{-}P(H)Mes\}]_3\bullet tol$	–4.13 - –4.08	b	9
$[Li(THF)_4]_2[(Cp'_2Dy)_3(\mu\text{-}PMes)_3Li]\bullet THF$	–2.702 - –2.749	b	9
$[Cp'_2Dy(\mu\text{-}Cl)]_2$	–4.81	b	10
$[Cp'_2Dy(\mu\text{-}Br)]_2$	–4.33	b	10
$[Cp'_2Dy(\mu\text{-}I)]_2$	–3.65	b	10
$[\{Dy(BH_4)_2(THF)\}_2(Fv^{tttt})]$	–0.9	b,c	11
$[Cp^*Dy(\mu\text{-}BH_4)\}_2(Fv^{tttt})]$	–2.5	b,c	11
$[(Cp^*Dy)_2(\mu\text{-}BH_4)(\eta^5\text{:}\eta^5\text{-}Fv^{tttt})]$	–1.4	b,c	11
$[Gd_2(Hhmb)_3(NCS)_3]\bullet 2MeOH\bullet py$	–0.02		12
$[GdL_3(H_2O)_1]_2$	0.05		13
$[Gd_4(HL)_4(\mu_2\text{-}MeO)_4]\bullet 4MeOH$	−0.105	d	14
$[Gd(Cy_3PO)_2(\mu\text{-}Br)(Br)_2]_2\bullet 2tol$	–0.029		15
$[Gd_2(L)(Cl\text{-salphen})_2]\bullet 0.5ClCH_2CH_2Cl$	−0.024	e	16
$Gd_2(thd)_6(4,4'\text{-Bpy})$	0.0491		17
$[Gd_4(LH)_4(LH_2)_2(MeO)_2]$	−0.033(1) −0.0133(3)	d	18

[a]Derived from CASSCF calculations; [b]Lines model; [c]Dipolar coupling; [d]Cluster complex; [e]Schiff base complex. Bpy = bipyridine, Cl-salphenH_2 = *N*,*N*′-bis(5-chlorosalicylidene)-*o*-phenylenediamine, Cp' = (η^5-C_5H_4Me), Fv^{tttt} = $[1,1',3,3'\text{-}(C_5{}^tBu_2H_2)_2]^{2-}$, Hhmb = *N*′-(2-hydroxy-3-methoxybenzylidene)benzhydrazide, HL = N′-(4-diethylamino-2-hydroxybenzylidene)-6-(hydroxymethyl)picolinohydrazide, L = salicylic acid, ind = indigo, LH = $C_{11}H_{13}N_3O_4$, Mes = mesityl, thd = 2,2,6,6-tetramethyl-3,5-heptanedione

5 Cyclic Voltammetry

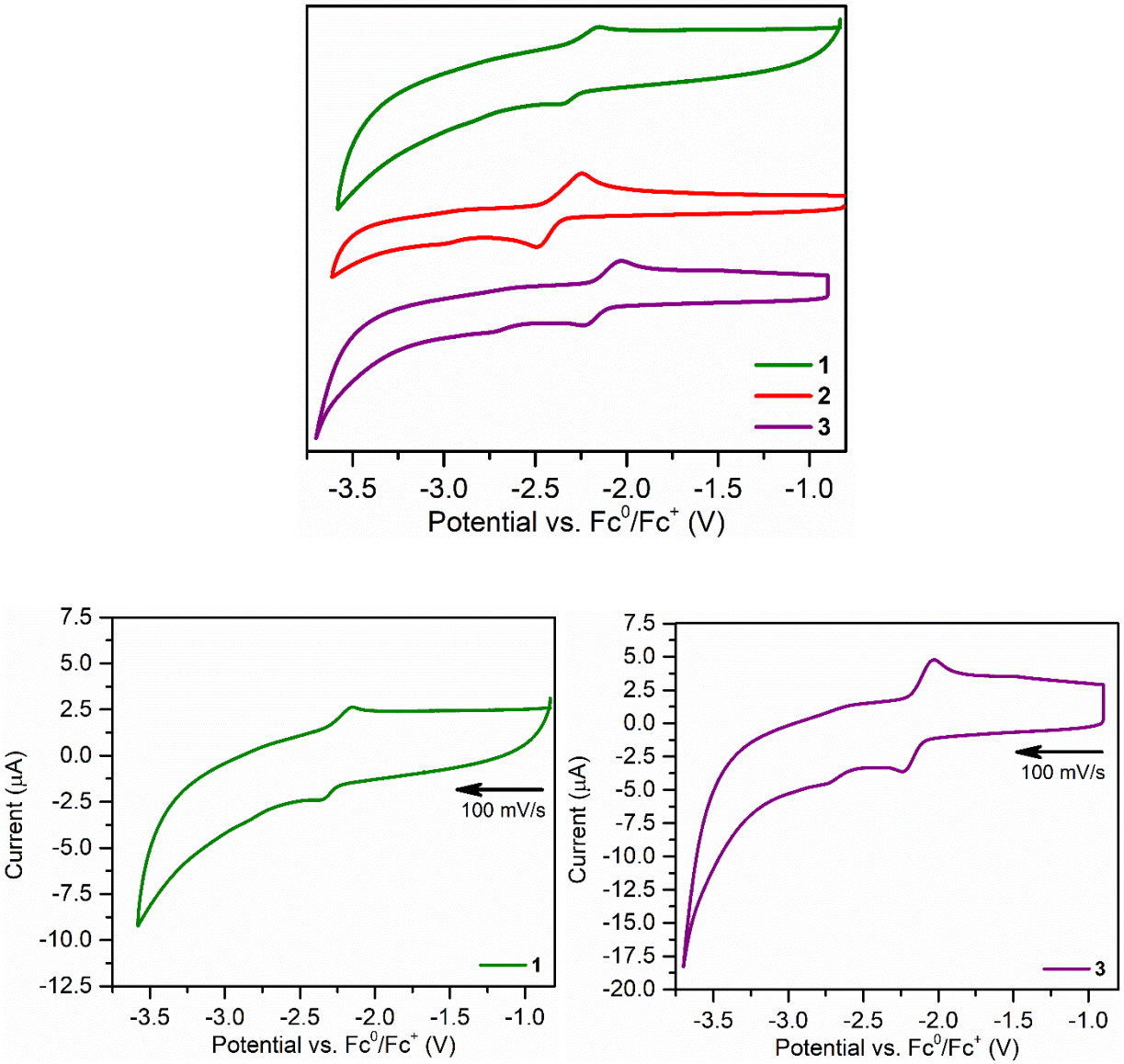

Fig S28. Cyclic voltammograms of $(Cp^*_2RE)_2(\mu\text{-}^{t\mathrm{Bu}}\text{salophen})$, where RE = Gd (**1**), Dy (**2**), and Y (**3**), measured in THF with $(^{n}Bu_4N)(PF_6)$ (1 mM) as an electrolyte and 100 mV/s scan rate (top). Magnification of the quasi-reversible features at –2.33 V of **1** (bottom left) and at –2.10 V of **3** (bottom right), respectively.

6 EPR Spectroscopy

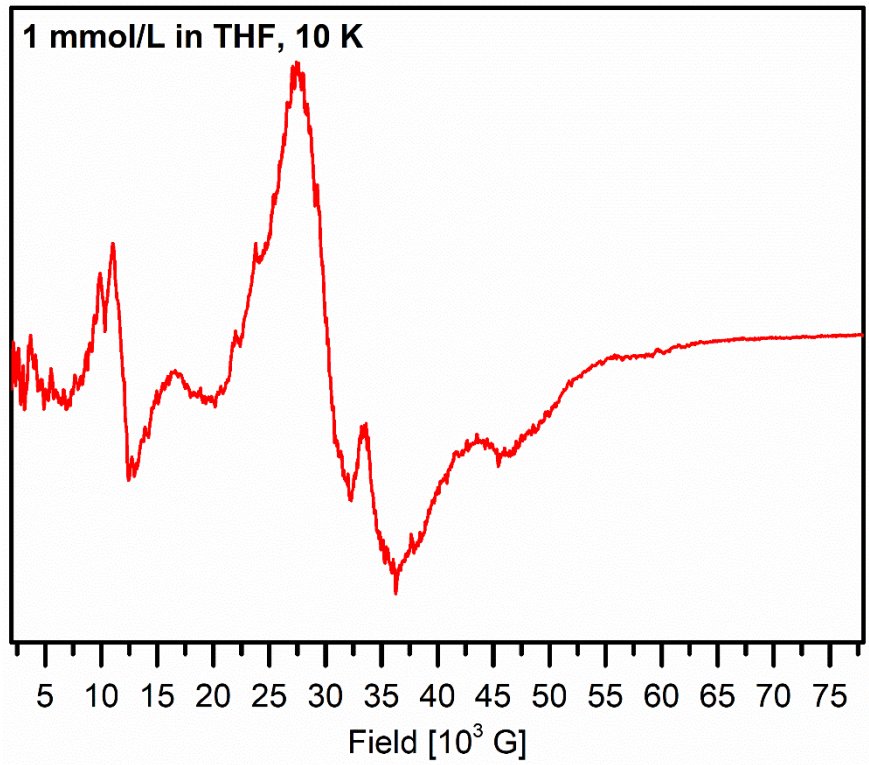

Fig. S29. Frozen solution X-band EPR spectrum of $(Cp^*_2Gd)_2(\mu\text{-}^{tBu}salophen)$, **1**, in THF, recorded at 10 K at 9.397 GHz with a 5.00 G modulation amplitude, 36.0 dB attenuation and a 60 dB gain.

7 DFT Calculations

Table S4. Metrical parameters for $(Cp^*_2Y)_2(\mu\text{-}^{t}Bu\text{salophen})$, **3**, calculated as a neutral singlet using the B3LYP functional with varying basis sets.

	Exp	def2-SV(P) 6-31+Gdp	def2-SV(P) 6-31Gdp	def2-SV(P)	def2-TZVP 6-311Gdp
			Distance (Å)		
Y1-Cp	2.6844	2.7176	2.7135	2.7136	2.7074
Y2-Cp	2.6915	2.7176	2.7136	2.7138	2.7076
Y1-O1	2.1679(15)	2.1890	2.1900	2.1870	2.1860
Y2-O2	2.1762(15)	2.1890	2.1900	2.1870	2.1860
Y1-N1	2.4471(18)	2.4610	2.4570	2.4590	2.4640
Y2-N2	2.4518(18)	2.4600	2.4570	2.4590	2.4640
O1-C21	1.309(3)	1.3050	1.3050	1.2980	1.3010
O2-C22	1.308(3)	1.3050	1.3050	1.2980	1.3010
N1-C24	1.309(3)	1.3110	1.3110	1.3100	1.3070
N2-C26	1.301(3)	1.3110	1.3110	1.3100	1.3070
N1-C23	1.435(3)	1.4240	1.4230	1.4200	1.4240
N2-C25	1.433(3)	1.4240	1.4230	1.4200	1.4240
C24-C52	1.438(3)	1.4360	1.4350	1.4370	1.4340
C26-C64	1.432(3)	1.4360	1.4350	1.4370	1.4340
MD		0.0073	0.0061	0.0047	0.0045
MSE		0.0002	0.0002	0.0002	0.0001
RMSE		0.0146	0.0134	0.0140	0.0120
MAPE		0.272%	0.216%	0.112%	0.111%

	Exp	def2-SV(P) 6-31+Gdp	def2-SV(P) 6-31Gdp	def2-SV(P)	def2-TZVP 6-311Gdp
			Angle (°)		
Cnt-Y-Cnt	**137.0**	137.408	137.571	137.907	137.556
N-Y-O	**76.1**	76.056	76.189	76.184	75.752
C-N-C	**117.4**	119.039	119.055	119.520	119.011
MD		0.647	0.751	1.017	0.586
MSE		0.946	1.013	1.760	1.010
RMSE		0.894	1.027	3.097	1.020
MAPE		0.522%	0.625%	0.837%	0.418%

[a]Mean deviation (MD). [b]Mean square error (MSE). [c]Root mean square error (RMSE). [d]Mean absolute percentage error (MAPE). [e]Cnt = Cp* ring centroid.

Table S5. Metrical parameters for $(Cp^*_2Y)_2(\mu\text{-}^{t}Bu\text{salophen})$, **3**, calculated as a neutral singlet using the hybrid TPSSh functional with varying basis sets.

	Exp	def2-SV(P) 6-31+Gdp	def2-SV(P) 6-31Gdp	def2-SV(P)	def2-TZVP 6-311Gdp
			Distances (Å)		
Y1-Cp	2.6844	2.6945	2.6919	2.6942	2.6825
Y2-Cp	2.6915	2.6945	2.6919	2.6941	2.6825
Y1-O1	2.1679(15)	2.1940	2.1950	2.1920	2.1900
Y2-O2	2.1762(15)	2.1940	2.1950	2.1920	2.1900
Y1-N1	2.4471(18)	2.4350	2.4340	2.4380	2.4360
Y2-N2	2.4518(18)	2.4350	2.4340	2.4380	2.4360
O1-C21	1.309(3)	1.3080	1.3080	1.3000	1.3040
O2-C22	1.308(3)	1.3080	1.3080	1.3000	1.3040
N1-C24	1.309(3)	1.3160	1.3160	1.3140	1.3120
N2-C26	1.301(3)	1.3160	1.3160	1.3140	1.3120
N1-C23	1.435(3)	1.4220	1.4210	1.4170	1.4210
N2-C25	1.433(3)	1.4210	1.4210	1.4170	1.4210
C24-C52	1.438(3)	1.4330	1.4320	1.4340	1.4310
C26-C64	1.432(3)	1.4330	1.4320	1.4330	1.4310
MD		0.0014	0.0009	-0.0005	-0.0022
MSE		0.0002	0.0002	0.0002	0.0001
RMSE		0.0124	0.0128	0.0124	0.0110
MAPE		0.066%	0.038%	0.081%	0.131%

	Exp	def2-SV(P) 6-31+Gdp	def2-SV(P) 6-31Gdp	def2-SV(P)	def2-TZVP 6-311Gdp
			Angles (°)		
Cnt-Y-Cnt	137.0	138.155	137.941	138.274	138.020
N-Y-O	76.1	76.215	76.279	76.238	75.958
C-N-C	117.4	118.260	118.665	119.140	118.565
MD		0.800	0.878	0.826	0.798
MSE		0.9704	1.0945	1.0695	0.7606
RMSE		0.985	1.046	1.034	0.872
MAPE		0.621%	0.696%	0.660%	0.644%

[a]Mean deviation (MD). [b]Mean square error (MSE). [c]Root mean square error (RMSE). [d]Mean absolute percentage error (MAPE). [e]Cnt = Cp* ring centroid.

Table S6. Metrical parameters for $(Cp^*_2Y)_2(\mu\text{-}^{t}Bu\text{salophen})$, **3**, calculated as a neutral singlet using the TPSSTPSS functional with varying basis sets.

	Exp	def2-SV(P) 6-31+Gdp	def2-SV(P) 6-31Gdp	def2-SV(P)	def2-TZVP 6-311Gdp
			Distances (Å)		
Y1-Cp	2.6844	2.6998	2.6976	2.6998	2.6884
Y2-Cp	2.6915	2.6999	2.6976	2.6999	2.6884
Y1-O1	2.1679(15)	2.1980	2.1990	2.1970	2.1950
Y2-O2	2.1762(15)	2.1980	2.1990	2.1960	2.1950
Y1-N1	2.4471(18)	2.4340	2.4320	2.4380	2.4350
Y2-N2	2.4518(18)	2.4340	2.4320	2.4380	2.4360
O1-C21	1.309(3)	1.3140	1.3140	1.3060	1.3100
O2-C22	1.308(3)	1.3140	1.3140	1.3060	1.3100
N1-C24	1.309(3)	1.3230	1.3230	1.3210	1.3190
N2-C26	1.301(3)	1.3230	1.3230	1.3210	1.3190
N1-C23	1.435(3)	1.4250	1.4240	1.4200	1.4240
N2-C25	1.433(3)	1.4250	1.4240	1.4200	1.4240
C24-C52	1.438(3)	1.4350	1.4340	1.4350	1.4320
C26-C64	1.432(3)	1.4350	1.4340	1.4350	1.4320
MD		0.0053	0.0045	0.0035	0.0017
MSE		0.0002	0.0002	0.0002	0.0002
RMSE		0.0149	0.0153	0.0141	0.0125
MAPE		0.312%	0.275%	0.166%	0.112%

	Exp	def2-SV(P) 6-31+Gdp	def2-SV(P) 6-31Gdp	def2-SV(P)	def2-TZVP 6-311Gdp
			Angles (°)		
Cnt-Y-Cnt	137.0	138.140	137.924	138.235	137.988
N-Y-O	76.1	76.464	76.518	76.480	76.178
C-N-C	117.4	118.616	118.604	119.071	118.528
MD		0.887	0.829	1.075	0.711
MSE		0.947	0.803	1.461	0.738
RMSE		0.896	0.645	2.136	0.544
MAPE		0.759%	0.727%	0.918%	0.572%

[a]Mean deviation (MD). [b]Mean square error (MSE). [c]Root mean square error (RMSE). [d]Mean absolute percentage error (MAPE). [e]Cnt = Cp* ring centroid.

8 References

1 N. F. Chilton, R. P. Anderson, L. D. Turner, A. Soncini and K. S. Murray, PHI: a powerful new program for the analysis of anisotropic monomeric and exchange-coupled polynuclear *d*- and *f*-block complexes, *J. Comput. Chem.*, 2013, **34**, 1164–1175.

2 J. D. Rinehart, M. Fang, W. J. Evans and J. R. Long, Strong exchange and magnetic blocking in N_2^{3-}-radical-bridged lanthanide complexes, *Nat. Chem.*, 2011, **3**, 538–542.

3 D. Errulat, B. Gabidullin, A. Mansikkamäki and M. Murugesu, Two heads are better than one: improving magnetic relaxation in the dysprosium metallocene upon dimerization by use of an exceptionally weakly-coordinating anion, *Chem. Commun.*, 2020, **56**, 5937–5940.

4 P. Evans, D. Reta, C. A. P. Goodwin, F. Ortu, N. F. Chilton and D. P. Mills, A double-dysprosocenium single-molecule magnet bound together with neutral ligands, *Chem. Commun.*, 2020, **56**, 5677–5680.

5 F. Tuna, C. A. Smith, M. Bodensteiner, L. Ungur, L. F. Chibotaru, E. J. L. McInnes, R. E. P. Winpenny, D. Collison and R. A. Layfield, A High Anisotropy Barrier in a Sulfur-Bridged Organodysprosium Single-Molecule Magnet, *Angew. Chem. Int. Ed.*, 2012, **51**, 6976–6980.

6 T. Pugh, N. F. Chilton and R. A. Layfield, Antimony-ligated dysprosium single-molecule magnets as catalysts for stibine dehydrocoupling, *Chem. Sci.*, 2017, **8**, 2073–2080.

7 F.-S. Guo and R. A. Layfield, Strong direct exchange coupling and single-molecule magnetism in indigo-bridged lanthanide dimers, *Chem. Commun.*, 2017, **53**, 3130–3133.

8 T. Pugh, V. Vieru, L. F. Chibotaru and R. A. Layfield, Magneto-structural correlations in arsenic- and selenium-ligated dysprosium single-molecule magnet, *Chem. Sci.*, 2016, **7**, 2128–2137.

9 T. Pugh, F. Tuna, L. Ungur, D. Collison, E. J. L. McInnes, L. F. Chibotaru and R. A. Layfield, Influencing the properties of dysprosium single-molecule magnets with phosphorus donor ligands, *Nat. Commun.*, 2015, **6**, 7492.

10 Y. Meng, J. Xiong, M. Yang, Y. Qiao, Z. Zhong, H. Sun, J. Han, T. Liu, B. Wang and S. Gao, Experimental Determination of Magnetic Anisotropy in Exchange-Bias Dysprosium Metallocene Single-Molecule Magnets, *Angew. Chem. Int. Ed.*, 2020, **59**, 13037–13043.

11 M. He, F.-S. Guo, J. Tang, A. Mansikkamäki and R. A. Layfield, Fulvalene as a platform for the synthesis of a dimetallic dysprosocenium single-molecule magnet, *Chem. Sci.*, 2020, **11**, 5745–5752.

12 A.-J. Hutchings, F. Habib, R. J. Holmberg, I. Korobkov and M. Murugesu, Structural Rearrangement Through Lanthanide Contraction in Dinuclear Complexes, *Inorg. Chem.*, 2014, **53**, 2102–2112.

13 J.-P. Costes, J. M. Clemente-Juan, F. Dahan, F. Nicodème and M. Verelst, Unprecedented Ferromagnetic Interaction in Homobinuclear Erbium and Gadolinium Complexes: Structural and Magnetic Studies, *Angew. Chem. Int. Ed.*, 2002, **41**, 323–325.

14 W.-M. Wang, M.-J. Wang, S.-S. Hao, Q.-Y. Shen, M.-L. Wang, Q.-L. Liu, X.-F. Guan, X.-T. Zhang and Z.-L. Wu, 'Windmill'-shaped Ln^{III}_4 (Ln^{III} = Gd and Dy) clusters: magnetocaloric effect and single-molecule-magnet behavior, *New J. Chem.*, 2020, **44**, 4631–4638.
15 M. Li, H. Wu, Z. Xia, V. Montigaud, O. Cador, B. Le Guennic, H. Ke, W. Wang, G. Xie and S. Chen, Bromine-bridged Dy_2 single-molecule magnet: magnetic anisotropy driven by cis/trans stereoisomers, *Chem. Commun.*, 2019, **55**, 14661–14664.
16 F. Gao, L. Wang, G.-Z. Zhu, Y.-H. Liu, H. Yang, X. Li and K. Yang, Controllable syntheses and magnetic properties of novel homoleptic triple-decker lanthanide complexes, *Dalt. Trans.*, 2019, **48**, 13360–13368.
17 X. Yao, G. An, Y. Li, P. Yan, W. Li and G. Li, Effect of nuclearity and symmetry on the single-molecule magnets behavior of seven-coordinated *β*-diketonate Dy(III) complexes, *J. Solid State Chem.*, 2019, **274**, 295–302.
18 M. U. Anwar, A. Al-Harrasi, J. M. Rawson, E. L. Gavey, J. Regier, D. Alexandropoulos, M. Pilkington and L. K. Thompson, Slow magnetic relaxation in Dy_2 and Dy_4 complexes of a versatile, trifunctional polydentate N,O-ligand, *Dalt. Trans.*, 2019, **48**, 14269–14278.